

The Roasting Marshmallows Program with IGRINS on Gemini South III: Seeing deeper into the metal depleted atmosphere of a gas-giant on the cusp of the hot to ultra-hot Jupiter transition

Vatsal Panwar^{1,2*}, Matteo Brogi^{3,4}, Krishna Kanumalla⁵, Michael R. Line⁵, Siddharth Gandhi^{1,2}, Peter C.B. Smith⁵, Jacob L. Bean⁶, Lorenzo Pino⁹, Arjun B. Savel⁷, Joost P. Wardenier⁸, Heather Cegla^{1,2,†}, Hayley Beltz⁷, Megan Weiner Mansfield^{5,7}, Jorge A. Sanchez⁵, Jean-Michel Désert¹⁰, Luis Welbanks⁵, Viven Parmentier¹¹, Changwoo Kye¹², Jonathan J. Fortney¹³, Tomás de Azevedo Silva⁹

¹Department of Physics, University of Warwick, Coventry, UK, CV47AL

²Center for Exoplanets and Habitability, University of Warwick, Coventry, UK, CV47AL

³Dipartimento di Fisica, Università degli Studi di Torino, via P. Giuria 1, Turin, I-10125, Italy

⁴Osservatorio Astrofisico di Torino, INAF, via Osservatorio 20, Pino Torinese, I-10025, Italy

⁵School of Earth & Space Exploration, Arizona State University, Tempe AZ 85287, USA

⁶Department of Astronomy & Astrophysics, University of Chicago, Chicago, IL, USA

⁷Department of Astronomy, University of Maryland, College Park, 4296 Stadium Dr., College Park, MD 207842 USA

⁸Institut Trottier de Recherche sur les Exoplanètes, Université de Montréal, Montréal, Québec, H3T 1J4, Canada

⁹INAF - Osservatorio Astrofisico di Arcetri, Florence, Italy

¹⁰Anton Pannekoek Institute for Astronomy, University of Amsterdam, P.O. Box 94249, Noord Holland, NL-1090GE Amsterdam, the Netherlands

¹¹Laboratoire Lagrange, Observatoire de la Côte d'Azur, CNRS, Université Côte d'Azur, Nice, France

¹²Department of Physics and Astronomy, Seoul National University, Seoul 08826, Korea

¹³Department of Astronomy and Astrophysics University of California, Santa Cruz, CA, USA

Accepted 2025 July 07. Received 2025 July 02; in original form 2025 March 19

ABSTRACT

Ultra-hot Jupiters (dayside temperatures $T_{\text{day}} > 2200$ K) are a class of gas-giant exoplanets that, due to extreme stellar irradiation, show a peculiar combination of thermochemical properties in the form of molecular dissociation, atomic ionization, and inverted thermal structures. Atmospheric characterization of gas giants lying in the transitional regime between hot and ultra-hot Jupiters can help in understanding the physical mechanisms that cause the fundamental thermochemical transition in atmospheres between the two classes of hot gas giants. Using high-resolution cross-correlation spectroscopy with the IGRINS spectrograph on Gemini South (1.4 to 2.5 μm), we present the day-side high-resolution spectrum of WASP-122b ($T_{\text{day}} = 2258 \pm 54$ K), a gas-giant situated at this transition. We detect the signal from H_2O , based on which we find that WASP-122b has a significantly metal-depleted atmosphere with metallicity $\log_{10}[\text{Z}_p/\text{Z}_\odot] = -1.48 \pm 0.25$ dex ($0.033^{+0.018}_{-0.016} \times$ solar), and solar/sub-solar C/O ratio = 0.36 ± 0.22 (3σ upper limit 0.82). Drastically low atmospheric metallicity pushes the contribution function to higher pressures, resulting in the planetary spectral lines to originate from a narrow region around 1 bar where the thermal profile is non-inverted. This is inconsistent with solar composition radiative convective equilibrium (RCTE) which predicts an inverted atmosphere with spectral lines in emission. The measured sub-solar metallicity and solar/sub-solar C/O ratio is inconsistent with expectations from core-accretion. We find the planetary signal to be significantly shifted in K_p and V_{sys} , which is in tension with the predictions from global circulation models and require further investigation. Our results highlight the detailed information content of high-resolution spectroscopy data and their ability to constrain complex atmospheric thermal structures and compositions of exoplanets.

Key words: exoplanets; planets and satellites: atmospheres; stars: solar-type

1 INTRODUCTION

The atmospheric thermal structures of irradiated gas-giant exoplanet atmospheres are determined by the interplay of stellar irradiation,

interior heat flux, and the opacity of atomic and molecular species in the atmosphere, which together govern the energy balance of the atmosphere (Seager & Sasselov 1998; Barman et al. 2005; Sudarsky et al. 2003; Burrows et al. 2007). The atmosphere of a hot gas-giant heats up by absorbing the incident stellar radiation typically in the visible wavelengths due to alkali (Na, K) and other refractory bearing species (e.g. TiO , VO), and cools by emitting radiation in the infrared

* E-mail: vatsal.panwar@warwick.ac.uk

† UKRI Future Leaders Fellow

wavelengths from molecules like H_2O , CO , and CO_2 . The resulting variation of temperature with altitude or pressure, often referred to as the pressure temperature ($P - T$) profile, is intimately connected to the atmospheric metallicity which controls the opacity of the atmosphere (Marley & Robinson 2015). Studies by Hubeny et al. (2003); Fortney et al. (2006, 2008) and more recently 3D global circulation model (GCM) simulations for a population of hot-Jupiters by Roth et al. (2024) have indicated that a fundamental change in the atmospheric opacity happens in the planetary equilibrium temperature range of $\sim 1700 - 2000$ K when TiO and VO , the main visible stellar light absorbers, exist in gas-phase and heat up the upper atmosphere causing thermal inversion (increasing temperature with altitude).

Ultra-hot Jupiters (Arcangeli et al. 2018; Mansfield et al. 2018; Kreidberg et al. 2018) are a class of even hotter gas-giants ($T_{\text{day}} > 2200$ K) for which a combination of high stellar irradiation and low-surface gravity causes most molecules, including TiO , VO and H_2O , to be thermally dissociated (Parmentier et al. 2018). The role of heating up the atmosphere in case of ultra-hot Jupiters is expected to be taken over by atomic species, e.g., resonant lines of Na I , K I , Mg I , Ca I at deeper pressures, and by Fe I and Fe II at lower pressures (Parmentier et al. 2018). The prevalence of thermally inverted $P - T$ profiles for ultra-hot Jupiters has been confirmed from numerous measurements of their emission spectra (Arcangeli et al. 2018; Mansfield et al. 2018; Pino et al. 2020; Mikal-Evans et al. 2022; Prinoth et al. 2022; van Sluijs et al. 2023; Smith et al. 2024; Pelletier et al. 2024; Deibert et al. 2024).

A combination of factors including surface gravity, equilibrium temperature, atmospheric composition, and stellar spectral type are expected to affect the onset and strength of thermal inversions across the hot and ultra-hot Jupiter population. For example, increasing the host star temperature (Lothringer & Barman 2019) and atmospheric metallicity (Parmentier et al. 2018) can both cause steeper (higher $\Delta T/\Delta P$ gradient of the temperature (T) - pressure (P) profile) thermal inversions. Analysis of a statistical sample of secondary eclipses of hot and ultra-hot Jupiters obtained through Spitzer Infrared Array Camera (IRAC) in the 3.6 and 4.5 μm photometric bandpasses and using the strength of CO emission feature as a proxy indicated that the transition to thermally inverted $P - T$ profile happens around 1700 K Baxter et al. (2020); Garhart et al. (2020). Investigations into the emission spectra of a sample of 19 hot and ultra-hot Jupiters obtained using Wide Field Camera 3 on the Hubble Space Telescope (HST/WFC3) by Mansfield et al. (2021) revealed a scatter in the strength of the 1.4 μm H_2O feature around the prediction from self-consistent atmospheric models, which could be explained as an outcome of rain-out of TiO/VO (for cooler hot-Jupiters) and variations in atmospheric metallicity and C/O ratio (for hotter hot-Jupiters).

There are ample theoretical predictions and corresponding observational evidence from broadband photometry and low to high resolution spectroscopy on the prevalence and causes for thermal inversion in the atmospheres of ultra-hot Jupiters. However, there are few observational constraints on the thermal structures of gas-giants in the parameter space between hot to ultra-hot Jupiters where this fundamental transition likely happens. WASP-122b/KELT-14b (Rodriguez et al. 2016; Turner et al. 2016) (hereafter referred to as WASP-122b) is one such hot-Jupiter ($T_{\text{eq}} \sim 1904 \pm 54$ K, $T_{\text{day}} = 2258 \pm 54$ K for redistribution efficiency $f = 1.98$) situated in this transition regime in the day-side temperature vs surface gravity space (Figure 1). Moreover, given its short orbital period (1.71 day), inflated size ($1.52 R_{\text{Jup}}$, $1.19 M_{\text{Jup}}$), and bright (K mag = 9.4) host star ($T_{\text{eff}} = 5800$ K, spectral type G4), it is an ideal candidate for emission spectroscopy (see Table 1 for system properties). It is a particularly favourable target for constraining its atmospheric thermal

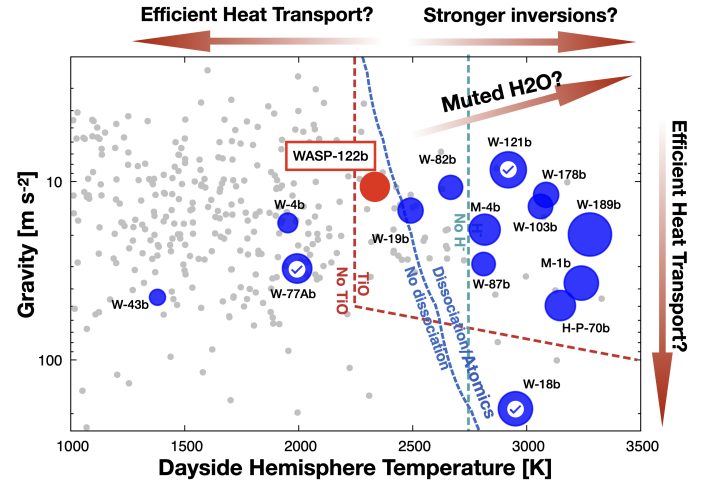


Figure 1. Surface gravity vs dayside temperature parameter space explored by the Roasting Marshmallows program to measure the dayside emission spectra of hot to ultra-hot Jupiters with IGRINS on Gemini South. General planet population is marked by grey symbols, and the planet names observed by the program in blue (W = WASP, and M = MASCARA, H-P = HAT-P). The symbol size is proportional to the S/N expected for each target relative to WASP-77 Ab. All the planets targeted by this survey span atmospheric transitions predicted by Parmentier et al. (2018) including onset of thermal inversions by TiO , and molecular thermal dissociation. The dayside temperatures plotted here were calculated assuming redistribution efficiency f predicted from the trend measured by Parmentier et al. (2021). Observations for planets marked by a white tick have been published already (Line et al. (2021); Brogi et al. (2023); Smith et al. (2024)). The focus of this work is the hot Jupiter WASP-122b ($T_{\text{day}} = 2258 \pm 54$ K for $f = 1.98$) which is situated in the transition regime between hot and ultra-Jupiter where the onset of thermal inversion is expected due to TiO/VO and molecular dissociation.

structure and metallicity through high-resolution cross-correlation spectroscopy (HRCCS; Snellen et al. (2010); Brogi et al. (2012); Birkby et al. (2013)). HRCCS uses high-resolution ($R > 15000$) time-series spectra and leverages the Doppler shift of many spectral lines induced by its orbital motion to disentangle the planetary atmospheric signal from telluric and stellar contamination. The technique is sensitive to line-shapes and contrasts (Birkby (2018)) and has been proven to obtain statistical constraints (Brogi & Line 2019; Gibson et al. 2020) on the vertical thermal structure and atmospheric compositions of hot to ultra-hot Jupiters (e.g. WASP-77 Ab Line et al. (2021); WASP-76b Gandhi et al. (2022); Weiner Mansfield et al. (2024); Pelletier et al. (2023); τ Boötis b Pelletier et al. (2021); Panwar et al. (2024); WASP-121b (Smith et al. 2024; Pelletier et al. 2025)). The precise constraints on elemental ratios of refractory and volatile species enabled by HRCCS have enabled linking the compositions of planetary atmospheres with their formation histories (Line et al. 2021; Smith et al. 2024; Pelletier et al. 2025). Phase resolved analyses of HRCCS signals have also revealed expected 3D signatures of dynamical processes like atmospheric circulation and drag in ultra-hot Jupiters (Beltz et al. (2021); Wardenier et al. (2024)).

In this work, we present the emission spectroscopy of the transitional hot Jupiter WASP-122b in the infrared H and K bands (1.4 to 2.4 μm) using the Immersion GRating INfrared Spectrometer (IGRINS, Mace et al. (2018) on Gemini-South) with the goal to constrain its atmospheric composition and thermal structure. We use our constraints on WASP-122b to investigate the role of atmospheric composition and stellar irradiation on the onset of thermal inversions in the regime between hot and ultra-hot Jupiters. We describe our

observations and data reduction and analysis steps in Section 2, followed by steps used to search for planetary spectral signatures and constraining the atmospheric abundances and P – T profile in Section 3 and 4 respectively. We discuss our findings and their implications in the context of thermal inversions in hot to ultra-hot Jupiters, and for the potential formation history of WASP-122b in Section 5, and summarize our conclusions in Section 6.

2 SPECTRAL EXTRACTION AND TELLURIC AND STELLAR DETRENDING

We observed WASP-122b for a single night on UTC 4th December 2023 with IGRINS on Gemini South as part of the Large-and-Long Program “Roasting Marshmallows: Disentangling Composition and Climate in Hot Jupiter Atmospheres through High-Resolution Thermal Emission Cross-Correlation Spectroscopy” (GS-2023B-LP-206, PI M. Line). The main goal of the program has been to conduct high spectral resolution phase-resolved cross-correlation spectroscopy of 15 hot Jupiters covering dayside temperatures 1400 – 2600 K, and diagnose the chemical, thermal, and dynamical mechanisms that drive key transitions in highly irradiated atmospheres. The observations of WASP-122b spanned 4.75 hours covering the pre-eclipse phase range 0.36 to 0.47 (corresponding to $T_0 = 2458654.016813 \pm 7 \times 10^{-5}$ BJD_{TDB} and orbital period $P_{\text{orb}} = 1.71005328 \pm 1.4 \times 10^{-7}$ from the most recent ephemeris measured by Kokori et al. (2023)). The observations were obtained as a continuous sequence of 39 AB pairs exposures (in ABBA nodding pattern, 324 seconds per AB sequence, which includes the exposure time for each A and B position and the overheads). The median signal-to-noise ratio (SNR) obtained per AB exposure was 70 and 65 in H and K bands.

The 1D spectra from all the exposures were extracted from the raw data using the IGRINS Pipeline Package (Lee & Gullikson 2016; Mace et al. 2018). Following the same steps as Line et al. (2021); Brogi et al. (2023); Smith et al. (2024), we apply additional corrections to the reduced 1D spectrum for each exposure, which involved trimming 100 pixels at start and end of each order, substituting any negative or NaN values from bad pixels to zero, removing orders heavily saturated by telluric absorption ($< 1.45 \mu\text{m}$, between $1.79 \mu\text{m}$ and $1.97 \mu\text{m}$, and $> 2.42 \mu\text{m}$). We re-aligned the spectrum for each exposure to the wavelength solution of the exposure with the highest SNR (hereafter reference spectrum). This was done by computing the least squares fit between each spectrum (with linear shift and stretch) for the wavelength solution as free parameters for each exposure) and the reference spectrum. For each exposure, we applied the best fit linear shift and stretch coefficients to the reference wavelength solution, and re-aligned the spectrum to this using B-spline interpolation. This yielded spectral datacubes with dimensions $N_{\text{order}} \times N_{\text{frame}} \times N_{\text{pixel}}$, where $N_{\text{order}} = 42$, $N_{\text{frame}} = 39$, and $N_{\text{pixel}} = 1848$.

We use principal component analysis (PCA) on an order by order basis to detrend the data and remove the telluric and stellar contamination. We follow the same procedure as described in Panwar et al. (2024), which we describe here in brief. We first standardize the datacubes of each order ($N_{\text{frame}} \times N_{\text{pixel}}$) by subtracting the mean flux and normalizing by the standard deviation for each spectral column. This ensures that noisier telluric channels are not overly weighted as compared to the rest of the spectral channels, while still letting PCA capture the required information to model the telluric channels. We then apply a Singular Value Decomposition (SVD) to the standardized datacube and compute a set of eigenvectors (also referred to as PCA vectors, each N_{frame} long) and their corresponding eigenvalues.

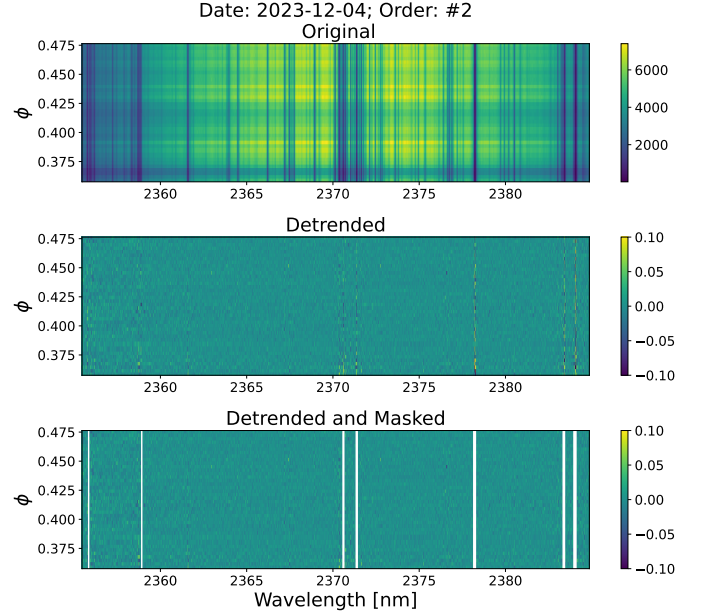


Figure 2. Demonstration of detrending the data to remove the contamination from stellar and telluric lines before cross-correlation. The top panel shows the original raw flux data cube where each row is the 1D spectrum for an exposure, the horizontal axis is the wavelength, and the vertical axis is the orbital phase for each exposure. The middle panel is the PCA detrended data cube. The bottom panel shows the same detrended data cube in the middle panel, but the spectral channels that still retain statistically significant level of residual noise have been masked out in white along with the bad pixels. The color bar in each panel represents measured flux in arbitrary linear units.

We use the eigenvalues to rank the PCA vectors in an order representing the amount of information encoded by them. Next, we append a unit vector to the set of PCA vectors, and perform a multi-linear regression on the original datacubes (before standardization) using a chosen number of PCA vectors from their ordered set (N_{PCA}), which yields a ‘fit’ to the dominant contribution from stellar and telluric systematics in a datacube. We then divide the original datacube by the fit, which yields the detrended datacube. We mask out any residual noisy columns in the detrended datacube in the same way as described in Section 2.2.1 of Panwar et al. (2024). An example of this process, which we repeat for each order, is shown in Figure 2.

The choice of N_{PCA} decides how aggressive the detrending is done, and using a high N_{PCA} runs the risk of removing part or whole of the planetary signal (e.g. Cheverall et al. (2023)). For the previously published IGRINS datasets from this program by Brogi et al. (2023); Smith et al. (2024), it has been found that fixing N_{PCA} to 4 to 6 performs well in terms of removing any visual telluric features, and the results are largely insensitive to the choice of N_{PCA} . After testing a range of values from 3 to 12, we find that beyond $N_{\text{PCA}} = 6$, the strength of the planetary signal (in terms of CCF S/N and log-likelihood derived confidence intervals, see Section 3) recovered is not strongly dependent on the choice of N_{PCA} . Hence, we fix to $N_{\text{PCA}} = 6$ for the remainder of this paper.

Table 1. Stellar and planetary parameters for WASP-122b/KELT-14b from [Rodriguez et al. \(2016\)](#) and [Turner et al. \(2016\)](#). The parameters from both are consistent with each other except the stellar radius and mass and hence the planetary radius and mass. This likely arises from the differences in stellar spectral analysis between the two studies. We use values from [Rodriguez et al. \(2016\)](#) for this work, and find that using values from [Turner et al. \(2016\)](#) do not change our results significantly.

Stellar Parameters		
Name	Rodriguez et al. (2016)	Turner et al. (2016)
R_{star}	$1.368 \pm 0.07 [R_{\odot}]$	$1.52 \pm 0.03 [R_{\odot}]$
M_{star}	$1.178 \pm 0.06 [M_{\odot}]$	$1.239 \pm 0.04 [M_{\odot}]$
$\log g_{\text{star}}$	$4.23 \pm 0.04 [\log_{10}[\text{cgs}]]$	$4.166 \pm 0.016 [\log_{10}[\text{cgs}]]$
T_{eff}	$5802 \pm 95 [\text{K}]$	$5750 \pm 120 [\text{K}]$
K mag	9.424 ± 0.023	–
V_{sys}	$34.62 \pm 0.13 [\text{km s}^{-1}]$	$34.59 \pm 0.002 [\text{km s}^{-1}]$
$v_{\text{S}} \sin i$	$7.7 \pm 0.4 [\text{km s}^{-1}]$	$3.3 \pm 0.8 [\text{km s}^{-1}]$
[Fe/H]	0.326 ± 0.09	0.32 ± 0.09
Planet Parameters (Literature)		
R_{p}	$1.52 \pm 0.11 [R_{\text{Jup}}]$	$1.74 \pm 0.05 [R_{\text{Jup}}]$
M_{p}	$1.196 \pm 0.07 [M_{\text{Jup}}]$	$1.284 \pm 0.03 [M_{\text{Jup}}]$
$\log g_{\text{p}}$	$3.107 \pm 0.07 [\log_{10}[\text{cgs}]]$	$3.02 \pm 0.01 [\log_{10}[\text{cgs}]]$
T_{eq}	$1904 \pm 54 [\text{K}]$	$1970 \pm 50 [\text{K}]$
T_0	$2457091.028632 \pm 4 \times 10^{-4} [\text{BJD}_{\text{TDB}}]$	$2456665.22401 \pm 2.1 \times 10^{-4} [\text{BJD}_{\text{TDB}}]$
P_{orb}	$1.7100588 \pm 2.5 \times 10^{-6} [\text{day}]$	$1.7100566 \pm 3.2 \times 10^{-6} [\text{day}]$
a	$0.02956 \pm 0.0005 [\text{A.U.}]$	$0.03005 \pm 0.0003 [\text{A.U.}]$
i	$79.67 \pm 0.8 [^{\circ}]$	$78.3 \pm 0.3 [^{\circ}]$
$(R_{\text{p}}/R_{\text{S}})^2$	0.01306 ± 0.0006	0.01386 ± 0.00029
Planet Parameters (Derived)		
K_{p}	$188.05 \pm 3.2 [\text{km s}^{-1}]$	$191.17 \pm 1.9 [\text{km s}^{-1}]$
$v_{\text{p}} \sin i$	$4.54 \pm 0.33 [\text{km s}^{-1}]$	$5.19 \pm 0.15 [\text{km s}^{-1}]$

3 SEARCH FOR MOLECULAR AND ATOMIC SPECIES USING CROSS-CORRELATION

We start with performing a search for the planetary signal by computing 2D cross-correlation maps ($K_{\text{p}} - V_{\text{sys}}$ maps) (e.g. [Brogi et al. \(2012\)](#); [De Kok et al. \(2013\)](#)) using a model emission spectrum for the planet’s atmosphere. We first describe the calculation of the model planetary emission spectrum, followed by steps to search for the signal in the data using cross-correlation.

We use the ScCHIMERA framework (as used in [Arcangeli et al. \(2018\)](#); [Piskorz et al. \(2018\)](#); [Mansfield et al. \(2018\)](#); [Line et al. \(2021\)](#)) to compute average day side pressure temperature ($P - T$) profiles and abundance (gas volume mixing ratio (VMR)) profiles corresponding to 1D radiative convective thermal equilibrium (1D-RCTE) for solar composition ($\text{C/O} = 0.55$, $\log_{10}[\text{Zp}/\text{Z}_{\odot}] = 0$), heat redistribution parameter $f = 1.98$ (based on the trend measured by [Parmentier et al. \(2021\)](#)), and planet parameters listed in Table 1. There are two set of planet parameters from the two discovery papers ([Rodriguez et al. \(2016\)](#); [Turner et al. \(2016\)](#)), most of which are consistent with each other within 1σ , except the planetary radius and mass. We note that the differences arise mainly from the significant differences in stellar radius and mass measured by the two works due to differences in their stellar spectral analysis. In this work, we choose to use both stellar and planetary parameters from [Rodriguez et al. \(2016\)](#) to be consistent, but we also checked and found that

using the [Turner et al. \(2016\)](#) parameters do not change our final results significantly.

We use the $P - T$ and VMR profiles from the 1D-RCTE model as inputs to GENESIS ([Gandhi & Madhusudhan 2017](#); [Pinhas et al. 2019](#)) to compute the 1D-RCTE planetary spectrum (F_{p}) at a constant resolution R ($\lambda/\Delta\lambda = 250000$). We include continuum opacities from collision induced absorption ($\text{H}_2\text{-H}_2$ and $\text{H}_2\text{-He}$), and H^- bound-free and H-e^- free-free absorption. We also include gas opacities from those atomic and molecular species which have predicted VMR from 1D-RCTE models is $> 10^{-7}$, have high cross-sections in the IGRINS wavelength range (taking values at 2000 K, 1 bar for reference), and for which reliably accurate and complete high-resolution opacity data are available. These include molecular, volatile and refractory bearing species: CO ([Rothman et al. 2010](#); [Li et al. 2015](#)), H_2O ([Polyansky et al. 2018](#)), CO_2 ([Huang et al. 2013, 2017](#)), OH ([Buldyreva et al. 2022](#)), TiO ([McKemmish et al. 2019](#)), FeH ([Bernath 2020](#)), MgO ([Buldyreva et al. 2022](#)), Fe I and Ti I ([Kurucz 2018](#)). We then rotationally broaden the F_{p} by convolving it with a rotation kernel corresponding to the projected line of sight planetary rotational velocity ($v_{\text{p}} \sin i$, assuming the planet to be tidally locked).

For the stellar spectrum (F_{S}), we take the high-resolution PHOENIX spectrum [Husser et al. \(2013\)](#), broaden it by a rotational kernel corresponding to the projected line of sight stellar rotational velocity ($v_{\text{S}} \sin i$), and smooth it using a Gaussian kernel with standard deviation of 200 elements. We also convolve both F_{p} and F_{S} to

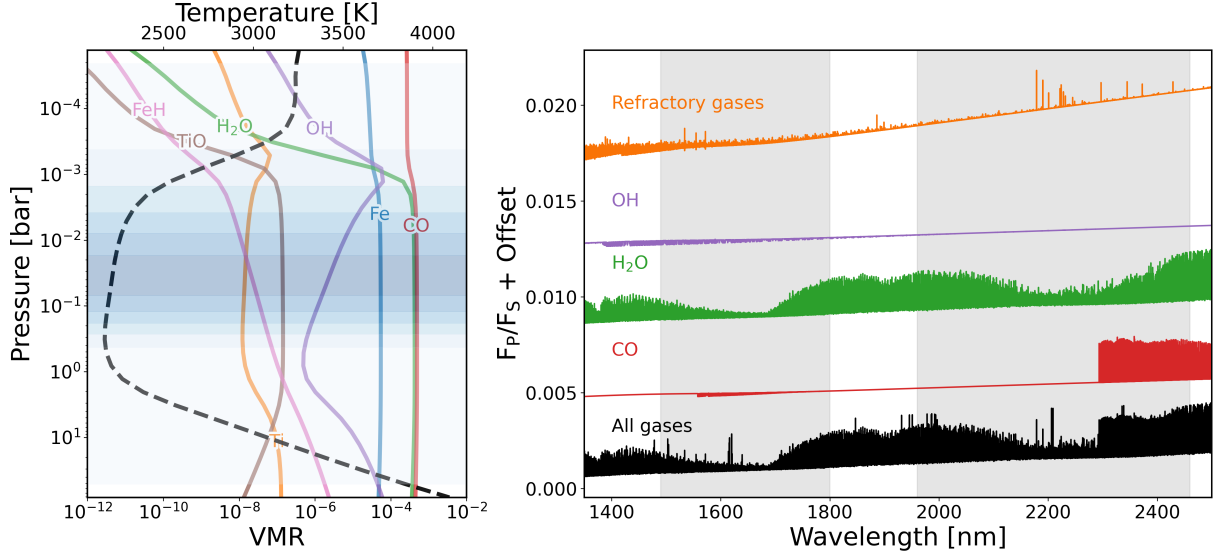


Figure 3. (Left panel) Vertical abundance (volume-mixing ratio (VMR)) profiles (solid lines) and P - T profile (dashed line) and the emission spectrum from all and individual molecular and atomic species as predicted from 1D radiative-convective thermal equilibrium (1D-RCTE) for WASP-122b. The shaded region in the left panel shows the wavelength integrated contribution function (Knutson et al. (2008)) calculated using GENESIS taking the VMR and P - T profiles from the ScCHIMERA 1D-RCTE model as input. (Right panel) Emission spectrum (ratio of planet flux F_P to the stellar flux F_S) corresponding to the 1D-RCTE VMR and P - T profiles calculated using GENESIS for all the species, and from selected individual molecular and refractory species, vertically shifted for clarity. C and O bearing species CO, H₂O, CO₂ and OH, and refractory bearing species (Fe I, Ti I, TiO, FeH) have detectable features in the IGRINS wavelength coverage (shaded region).

the instrumental resolution of IGRINS, assuming a Gaussian kernel for the instrument's line-spread function with the full-width half-maxima (FWHM) equivalent to the ratio of the model resolution ($R = 250000$) to the instrument resolution ($R = 45000$). We assume the IGRINS resolution to be constant across the wavelength range.

The planet to star contrast F_P/F_S (hereafter referred to as the model spectrum), which we eventually use to perform the cross-correlation, is computed as the ratio of rotationally and instrumentally broadened F_P and F_S (including scaling by the ratio of planet-to-stellar disk area ($(R_P/R_S)^2$)). The 1D-RCTE P - T and VMR profiles, and the corresponding planet to star contrast F_P/F_S from all species and individual molecular and refractory species are shown in Figure 3. The 1D-RCTE predicts an inverted P - T profile, with a steep inversion at pressures lower than 0.001 bar, and weaker inversion at higher pressure ranges of 0.5 to 0.15 bar where the peak contribution to the model spectrum comes from based on the wavelength integrated contribution function (Griffith et al. 1998; Knutson et al. 2008). The model spectrum as a consequence shows spectral features in emission, with dominant contribution from CO, H₂O, and refractory species.

We follow the conventional steps common in literature and also described in more detail in Panwar et al. (2024) to compute the K_P - V_{sys} map for the cross-correlation function (CCF), which we describe here in brief along with some differences. Before cross-correlating the model spectrum, we describe the steps we follow to first construct the time and wavelength dependent model spectrum cube $F_P/F_S(\phi, \lambda)$ that accounts for the Doppler shift of the stellar and planetary spectrum in the observer's rest frame. The line-of-sight velocity of the planet in the rest frame of the observer, assuming a circular orbit, can be described as:

$$V_P(\phi) = K_P \sin(2\pi\phi) + V_{\text{sys}} + V_{\text{bary}}(\phi) \quad (1)$$

whereas the line-of-sight velocity for the star is:

$$V_S(\phi) = V_{\text{sys}} + V_{\text{bary}}(\phi) + K_S \quad (2)$$

where ϕ is the planetary orbital phase which is a function of time, K_P is the Keplerian velocity semi-amplitude of the planet, V_{sys} is the radial velocity of the planet and star system with respect to the barycentre of the solar system, K_S is the Keplerian velocity of the star, and $V_{\text{bary}}(\phi)$ is the barycentric earth radial velocity (BERV) with respect to the observatory's rest frame. For a hot Jupiter like WASP-122b, K_S is of the order of ~ 100 m/s, which is negligible and quasi-stationary in the comparison to the planetary velocity ~ 100 km/s. We construct $F_P/F_S(\phi, \lambda)$ by Doppler shifting $F_P(\lambda)$ and $F_S(\lambda)$ by $V_P(\phi)$ and $V_S(\phi)$ respectively (Equations 1 and 2) and taking their ratio (calculation of $F_P(\lambda)$ and $F_S(\lambda)$ includes scaling by $(R_P/R_S)^2$). To emulate the effect of PCA detrending on the planetary signal in the data, we perform model reprocessing on $F_P/F_S(\phi, \lambda)$ using the same steps as described in Panwar et al. (2024). This involves first creating model injected data cube $F_{\text{data+model}}$ by injecting $F_P/F_S(\phi, \lambda)$ into the original data cube F_{data} (before PCA detrending) for a given pair of K_P and V_{sys} values:

$$F_{\text{data+model}}(\phi, \lambda) = F_{\text{data}}(\phi, \lambda)(1 + F_P/F_S(\phi, \lambda)) \quad (3)$$

We then detrend $F_{\text{data+model}}$ using exactly the same set of PCA eigenvectors and steps used to detrend F_{data} , and obtain the reprocessed model $F_P/F_S(\phi, \lambda)_{\text{reprocess}}$ as:

$$F_P/F_S(\phi, \lambda)_{\text{reprocess}} = F_{\text{data+model, detrend}}(\phi, \lambda) - F_{\text{data, detrend}}(\phi, \lambda) \quad (4)$$

We compute the CCF K_P - V_{sys} maps per order by computing the cross-correlation (cross-covariance normalized by the variances) between the reprocessed model spectrum $F_P/F_S(\phi, \lambda)_{\text{reprocess}}$ and

the data cube frame by frame (i.e. for each ϕ) for a grid of K_p and V_{sys} values with step size of 1 km s^{-1} . We sum the CCF across all frames to obtain the map for each order, which we then sum across all orders to obtain the total $K_p - V_{\text{sys}}$ map. We compute the signal-to-noise of the peak by first sigma-clipping any outliers in the map beyond 3σ threshold, followed by subtracting the median of all the values outside the $\pm 10 \text{ km s}^{-1}$ of the peak within which the signal is localized. We then normalize the median subtracted map by the standard-deviation of all values outside the $\pm 10 \text{ km s}^{-1}$ of the peak, resulting in the map for CCF S/N shown in Figure 4. We also use the CCF to log-likelihood framework introduced by Brogi & Line (2019) to construct the corresponding log-likelihood derived confidence interval map. This is an alternative way to assess the significance of CCF by computing the confidence intervals for the map using the log-likelihood and assuming 2 degrees of freedom corresponding to the two velocities K_p and V_{sys} (see Panwar et al. (2024) for more details of the steps). The resulting CCF S/N and confidence interval $K_p - V_{\text{sys}}$ map for the 1D-RCTE model is shown in Figure 4.

On inspecting the CCF S/N map for the 1D-RCTE model, we find that instead of a positive peak in the CCF at the expected K_p and V_{sys} there is an anticorrelated peak with S/N $\sim 3\sigma$ offset by $\sim +35 \text{ km s}^{-1}$ and -17 km s^{-1} in K_p and V_{sys} respectively. This indicates that there is a mismatch in the shape and contrast of the spectral lines in the solar composition ($C/O = 0.55$, $\log_{10}Z = 0$) 1D-RCTE model spectrum and the planetary signal present in the data. The 1D-RCTE model spectrum has an inverted profile, with all the spectral lines in emission, whereas it is likely that the spectral lines in the data are either all or partly in absorption, which could be causing the anticorrelated signal in the CCF map. We illustrate this dichotomy in Figure 5 by computing spectra from solely inverted and non-inverted $P - T$ profiles for WASP-122b, assuming a simple linear gradient in temperature with pressure and solar composition. A solely inverted profile shows all spectral lines in emission, whereas solely non-inverted profile shows all lines in absorption. The anticorrelated peak in the $K_p - V_{\text{sys}}$ map implies that a solar composition 1D-RCTE model is an incorrect description of the atmosphere, and there are variations in the $P - T$ profile and atmospheric abundance that need to be investigated to figure out the scenario that best matches the planetary signal in the data. In the next section, we do this by performing an atmospheric retrieval, which searches across models with a range of atmospheric abundances and thermal structures, to find the best fit atmospheric model in the context of the data, along with statistical constraints on the model parameters.

4 RETRIEVING THE ATMOSPHERIC COMPOSITION AND THERMAL STRUCTURE

We move towards obtaining statistical constraints on the composition and thermal structure of WASP-122b's dayside by using the CCF to log-likelihood mapping framework from Brogi et al. (2017) to perform Bayesian inference (commonly referred to as an atmospheric retrieval). This involves parametrizing the forward model spectrum calculated using GENESIS (as described in Section 3) by parametrizing the Doppler shift (through K_p and V_{sys}), and the gas VMR and $P - T$ profiles.

We follow the two common methods to parametrize the gas VMR profiles in the literature: 1) assuming free chemistry (e.g. Line et al. (2013)), where the VMR of each gas is assumed to be vertically constant and is a free parameter, and 2) assuming equilibrium chemistry (e.g. Brogi et al. (2023); Smith et al. (2024)), where the VMR pro-

file of each gas is calculated assuming equilibrium chemistry using FastChem (Stock et al. 2018, 2022). FastChem takes inputs in the form of $P - T$ profile, metallicity ($\log_{10}(Z_p/Z_\odot)$), Z_p is the planet metallicity, Z_\odot is the solar metallicity), and C/O ratio, and calculates abundance profiles for chemical species accounting for dissociation, ionization, and condensation. For each FastChem calculation, we use the value of the planet metallicity relative to solar composition ($\log_{10}(Z_p/Z_\odot)$) to scale the abundances of all elements first, and then use the value of C/O to scale the abundance of Carbon relative to Oxygen.

We employ a slight variation to the free chemistry setup by considering the VMR of all species constant with pressure except H_2O . For H_2O , we expect significant thermal dissociation onset around 1 mbar as indicated by the RCTE model (as shown in Figure 3). Hence, we use the empirical power law coefficients presented by Parmentier et al. (2018) to prescribe the H_2O VMR profile accounting for thermal dissociation, fixing all the parameters except the deep abundance of H_2O which we fit for in the retrieval.

For both free and equilibrium chemistry retrievals, we follow the same setup for GENESIS as described in Section 3 to compute the forward model spectrum cube $F_p/F_s(\phi, \lambda)$ along with model reprocessing, and considering contributions from the following molecules: CO, H_2O , OH, H_2S , TiO, FeH, MgO, and atomic species: Fe and Ti. We also include continuum opacities from collision induced absorption ($\text{H}_2 - \text{H}_2$ and $\text{H}_2 - \text{He}$), and H^- bound-free and H-e^- free-free absorption. We choose to use the 6 parameter Bézier spline parametrization for the $P - T$ profile, as introduced by Smith et al. (2024). This involves defining four points or nodes: $(\log_{10}P_0, T_0)$, $(\log_{10}P_1, T_1)$, $(\log_{10}P_2, T_2)$, $(\log_{10}P_3, T_3)$; $\log_{10}P_0 > \log_{10}P_1 > \log_{10}P_2 > \log_{10}P_3$, in the pressure-temperature space and using them as control points to compute a Bézier curve, which is then interpolated onto the pressure grid of GENESIS, which in this work we consider as 50 layers spaced linearly in log-space between 10^{-6} to 10^2 bar. We fix the pressure values for two nodes to the bottom ($\log_{10}P_0 [\text{bar}] = 2$) and top of the atmosphere ($\log_{10}P_3 [\text{bar}] = -6$), which leaves 6 free parameters: $T_0, \log_{10}P_1, T_1, \log_{10}P_2, T_2, T_3$. This Bézier spline parametrization provides a balance between the flexibility in the shape of the profile and the number of free parameters needed to describe it. It allows for both a monotonically inverted or non-inverted $P - T$ profile, and a mix of both in the lower and upper of the atmospheres. The latter is especially relevant in the case of WASP-122b, as we discuss in more detail in Section 5.1.

The total set of free parameters and their priors for both the equilibrium and free chemistry retrievals are shown in Table 2 and 4 respectively. We run the retrieval using our code `crocodile`¹ which couples the parametrized log-likelihood calculation with the nested sampling algorithm MultiNest (Feroz et al. 2009) implemented as pymultinest (Buchner et al. 2014) to compute the marginalized posterior distributions for the free model parameters. We run MultiNest with the number of live points set to 1000, and a tolerance on the Bayesian evidence (Z) as $\Delta \ln Z = 0.5$. The retrieval converges when the tolerance on $\Delta \ln Z$ is reached, with ~ 100000 log-likelihood evaluations, resulting in 8822 and 11934 equal weighted posterior samples for the free and equilibrium chemistry cases respectively.

We summarize the results from the equilibrium and free chemistry retrievals in the brief corner plots shown in Figures 6 and 8 respectively. The full corner plots for all the parameters are shown in Figures A1 and A2. Table 2 and 4 list the best fit and 1σ constraints obtained for each free parameter from the two retrievals. We also

¹ <https://github.com/vatsalpanwar/crocodile>

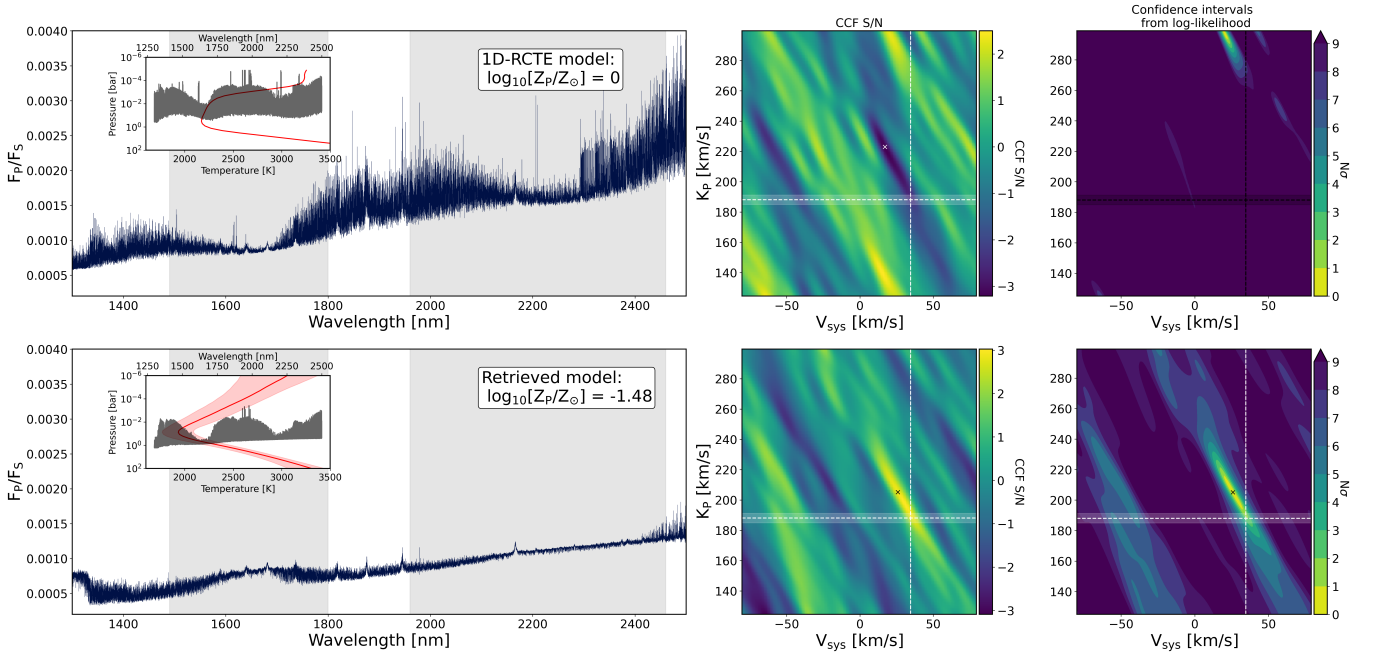


Figure 4. Model emission spectrum (F_p/F_s) and the corresponding K_p - V_{sys} maps for the CCF and log-likelihood derived confidence intervals for the 1D-RCTE model (top row) and the retrieved model (bottom row). In the inset are shown the P - T profiles for both cases, with the wavelength dependent photosphere (pressures corresponding to $\tau = 2/3$ for a given wavelength) overplotted in grey along duplicate X-axis. The solar composition 1D-RCTE model has the photosphere spanning mostly the inverted part of the P - T profile, causing all spectral lines to be in emission. In contrast, the retrieved model with ~ 1.5 dex sub-solar metallicity has a deeper photosphere spanning both non-inverted and inverted region of the P - T profile, causing the spectral lines to be both in absorption (blue end of the spectrum) and emission (redder end of the spectrum). The best fit retrieved model shows a 3σ peak in the CCF S/N K_p - V_{sys} map (bottom panel, second column), and the log-likelihood derived confidence interval map (bottom panel, third column) show a clear detection with the 3σ interval tightly constrained but the peak of the signal (marked by 'x') shifted from the expected K_p and V_{sys} values (marked by dashed lines).

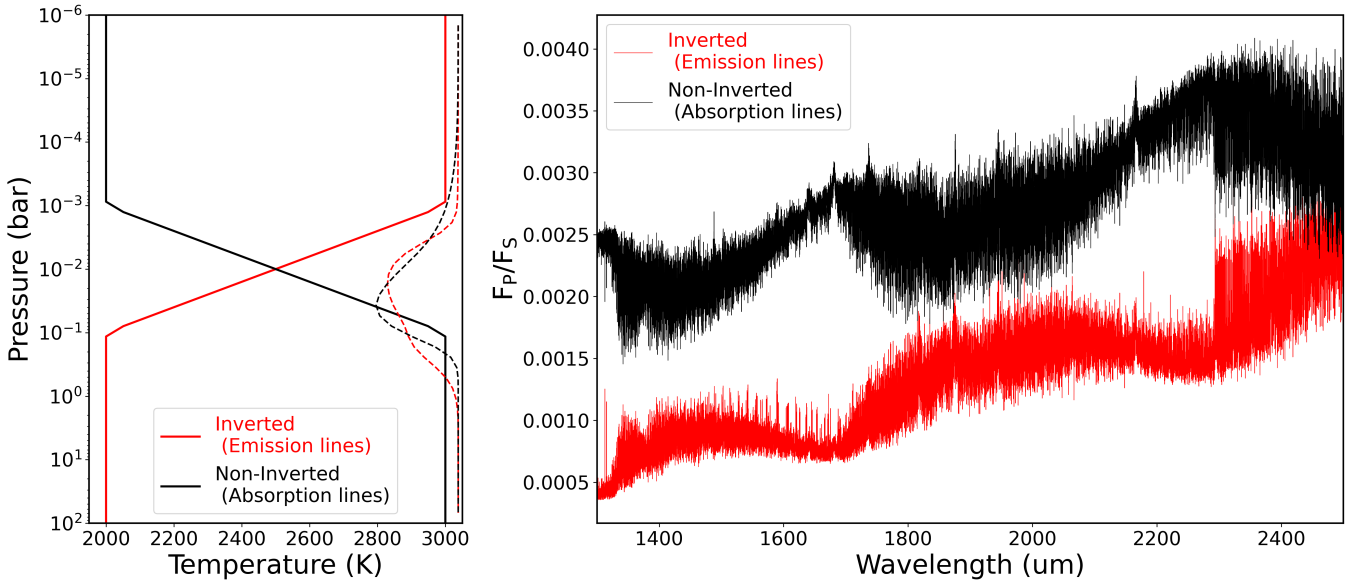


Figure 5. Dichotomy between inverted and non-inverted P - T profiles (left panel) and the shape of lines in the corresponding spectra (right panel), both assuming solar composition, with an arbitrary vertical offset between them for clarity. The solid lines in the left panel show two fully inverted (red) and fully non-inverted (black) P - T profiles prescribed as a linear temperature gradient between two points in the atmosphere. Their respective wavelength integrated contribution functions, assuming solar composition for both, are shown in dashed curve. The inverted profile leads to all spectral lines in emission (right panel), whereas the non-inverted profile yields all spectral lines in absorption.

Table 2. Best fit and 1σ values for the parameters from equilibrium chemistry retrieval, assuming 4 node Bézier spline P – T parametrization.

Parameter	Prior Bounds	Best fit $\pm 1\sigma$
K_P (km s $^{-1}$)	[160.00, 250.00]	$205.16^{+7.35}_{-7.61}$
V_{sys} (km s $^{-1}$)	[5.00, 50.00]	$25.86^{+4.49}_{-4.24}$
T_0 [K]	[400.00, 3500.00]	$3315.36^{+132.87}_{-248.52}$
T_1 [K]	[400.00, 3500.00]	$1402.91^{+936.04}_{-699.01}$
$\log_{10}P_1$ [bar]	[-6.00, 2.00]	$-2.58^{+0.92}_{-1.09}$
T_2 [K]	[400.00, 3500.00]	$1532.01^{+979.88}_{-730.66}$
$\log_{10}P_2$ [bar]	[-6.00, 2.00]	$1.44^{+0.41}_{-0.86}$
T_3 [K]	[400.00, 3500.00]	$3069.83^{+299.21}_{-482.52}$
$\log_{10}[Z_P/Z_\odot]$	[-6.00, 2.00]	$-1.48^{+0.26}_{-0.22}$
C/O	[0.00, 2.00]	$0.36^{+0.23}_{-0.22}$

Table 3. Best fit and 1σ values for the parameters from equilibrium chemistry retrieval, assuming linear gradient P – T with no inversion.

Parameter	Prior Bounds	Best fit $\pm 1\sigma$
K_P (km s $^{-1}$)	[160.00, 250.00]	$205.57^{+7.86}_{-7.65}$
V_{sys} (km s $^{-1}$)	[5.00, 50.00]	$25.80^{+4.27}_{-4.40}$
$\log_{10}P_1$ [bar]	[-1.00, 7.00]	$0.55^{+5.45}_{-4.59}$
T_1 [K]	[400.00, 3500.00]	$3044.69^{+320.58}_{-368.34}$
$\log_{10}P_2$ [bar]	[-1.00, 7.00]	$-0.31^{+5.16}_{-4.83}$
T_2 [K]	[400.00, 3500.00]	$1975.39^{+196.09}_{-205.74}$
$\log_{10}[Z_P/Z_\odot]$	[-6.00, 2.00]	$-1.66^{+0.27}_{-0.26}$
C/O	[0.00, 2.00]	$0.27^{+0.24}_{-0.19}$

tested the sensitivity of retrievals to the choice of N_{PCA} , by repeating the equilibrium chemistry retrieval for a range of values for N_{PCA} = (4, 5, 6, 7, 8). We find that the constraints on the abundances and the P – T profile obtained from the retrievals with varying N_{PCA} are consistent with each other within 1σ , whereas the velocities (K_P , and V_{sys}) are consistent within 2σ .

4.1 Constraints on the Abundances and Thermal Structure of WASP-122b

We find that both free and equilibrium chemistry retrievals successfully converge and constrain the K_P and V_{sys} velocities and the P – T profile. In particular, the posteriors from the equilibrium chemistry retrieval (Figure 6) indicates a significantly metal-depleted atmosphere with $\log_{10}[Z_P/Z_\odot] = -1.48^{+0.25}_{-0.22}$ dex, which translates to $0.033^{+0.018}_{-0.016} \times$ solar metallicity. We find solar/sub-solar C/O ratio = $0.36^{+0.22}_{-0.22}$ (3σ upper limit 0.82) consistent with solar C/O ratio of 0.55 [Asplund et al. \(2021\)](#). This agrees with results from the free chemistry retrieval which finds a ~ 2 dex sub-solar abundance for H_2O $\log_{10}(\text{H}_2\text{O}) = -4.86^{+0.14}_{-0.13}$ with a non-detection of CO, OH (Figure 8) and all the refractory species (Figure A2).

We find that some refractory and refractory bearing species like Fe, MgO, and Ti show peaks in their posterior distribution (see Fig-

Table 4. Best fit and 1σ values for the parameters from free chemistry retrieval, assuming 4 node Bézier spline P – T parametrization.

Parameter	Uniform Prior Bounds	Best fit $\pm 1\sigma$
K_P (km s $^{-1}$)	[160.00, 250.00]	$204.08^{+4.74}_{-4.92}$
V_{sys} (km s $^{-1}$)	[5.00, 50.00]	$26.34^{+2.92}_{-2.74}$
T_0 [K]	[400.00, 3500.00]	$3370.89^{+94.28}_{-176.69}$
T_1 [K]	[400.00, 3500.00]	$1253.08^{+949.41}_{-596.67}$
$\log_{10}P_1$ [bar]	[-6.00, 2.00]	$-2.92^{+0.97}_{-1.04}$
T_2 [K]	[400.00, 3500.00]	$1679.11^{+938.82}_{-740.91}$
$\log_{10}P_2$ [bar]	[-6.00, 2.00]	$1.59^{+0.29}_{-0.59}$
T_3 [K]	[400.00, 3500.00]	$3217.55^{+191.18}_{-286.41}$
$\log_{10}[\text{CO}]$	[-15.00, -1.00]	$-9.77^{+3.65}_{-3.42}$
$\log_{10}[\text{H}_2\text{O}]$	[-15.00, -1.00]	$-4.86^{+0.14}_{-0.13}$
$\log_{10}[\text{OH}]$	[-15.00, -1.00]	$-11.04^{+2.54}_{-2.52}$
$\log_{10}[\text{FeH}]$	[-15.00, -1.00]	$-11.50^{+2.20}_{-2.21}$
$\log_{10}[\text{TiO}]$	[-15.00, -1.00]	$-10.94^{+2.68}_{-2.59}$
$\log_{10}[\text{MgO}]$	[-15.00, -1.00]	$-10.25^{+1.24}_{-3.02}$
$\log_{10}[\text{Fe}]$	[-15.00, -1.00]	$-2.44^{+0.91}_{-7.21}$
$\log_{10}[\text{Ti}]$	[-15.00, -1.00]	$-6.68^{+0.98}_{-4.72}$
$\log_{10}\text{H}^-$	[-15.00, -1.00]	$-12.62^{+1.49}_{-1.48}$

ure A2), but the overall distribution has a finite tail towards lower abundances up to the lower bound of the prior, which indicates that these species are unconstrained by the retrieval. We also find that the vertical abundance profiles constrained from the equilibrium chemistry retrieval are consistent with the constraints on the vertically uniform abundances from the free chemistry retrieval, as shown in Figure 9. We also ran a free chemistry retrieval with the same setup but without Fe and Ti and find negligible support for model with Fe and Ti (Bayes factor based on Bayesian evidence (Z) between the two models is $\Delta \ln Z \sim 1$).

Similar to the steps followed in previous studies (e.g. [Panwar et al. \(2024\)](#); [Brogi et al. \(2023\)](#)) we also derived the posteriors for atmospheric metallicity $\log_{10}[Z_P/Z_\odot]$ from the free chemistry retrieval as shown in Figure 14. We considered only the posterior samples with CO abundance above -6.5 dex, because for smaller values of CO abundance the derived posterior for C/O gets heavily piled up at values close to 0, making it difficult to estimate the upper limit. We find that the derived posteriors from the free chemistry retrieval indicate the $\log_{10}[Z_P/Z_\odot] = -1.78^{+0.34}_{-0.22}$ (driven by planetary O/H measured through detection of H_2O), and 3σ upper limit on C/O = 0.91. This is consistent with the constraints on $\log_{10}[Z_P/Z_\odot]$ and the upper limit on the C/O ratio obtained from the equilibrium chemistry retrieval. The Bayes factor between the free and equilibrium chemistry is negligible, implying no strong preference for either ($\Delta \ln Z \sim 0.4$).

The P – T profile constrained by both the retrievals are also consistent with each other well within 1σ (see inset in Figures 6 and 8). Note that the free-parameters for our P – T parametrization are the three pressure and temperature nodes ($\log_{10}P$, T) for the Bézier spline parametrization, and the nodes themselves do not lie on the P – T profile but are used as control points to compute the P – T profile for a given range of pressures. Hence, while the posteriors for

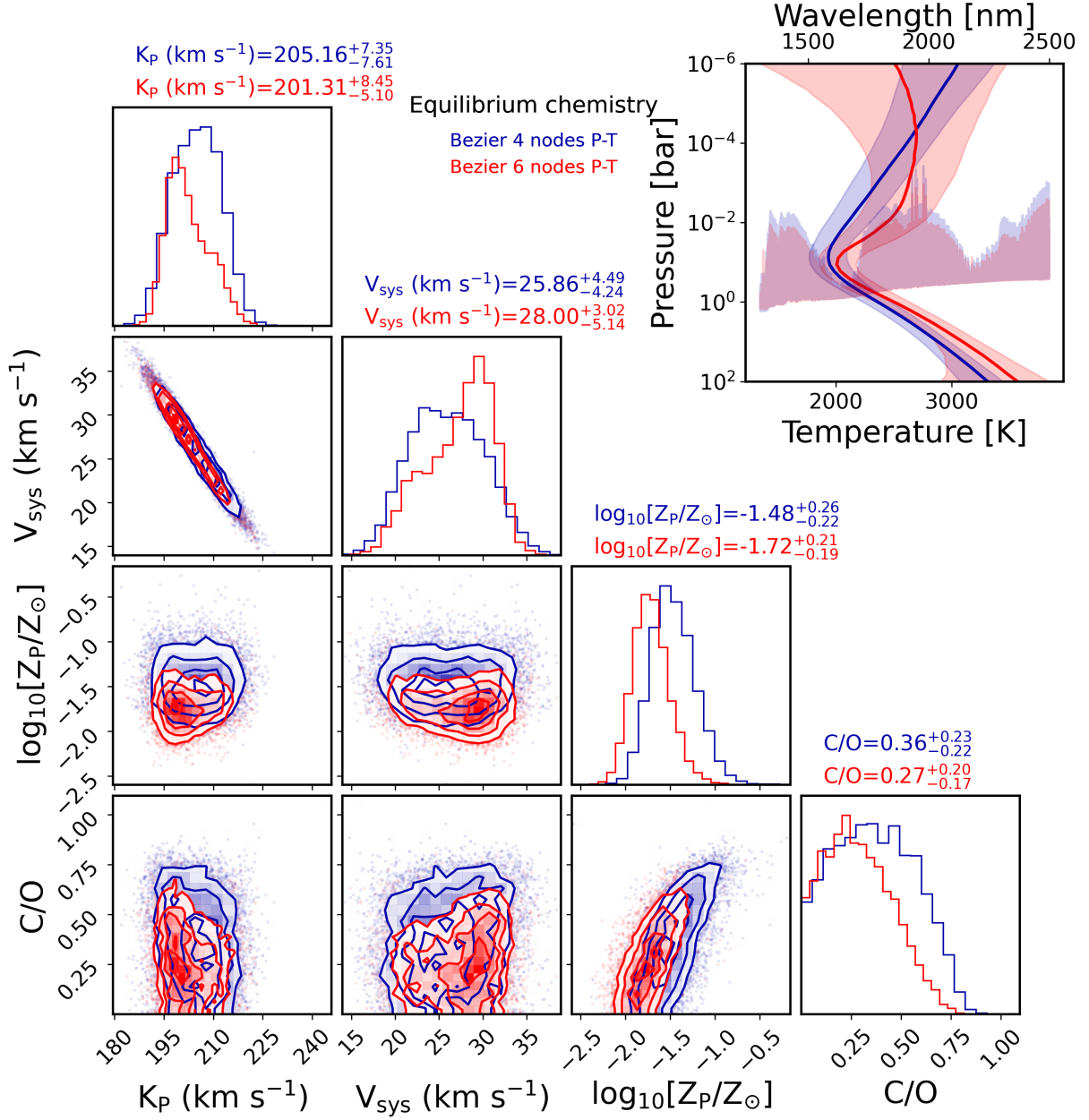


Figure 6. Cornerplot showing the 1D and 2D posterior distributions for some of the free parameters constrained by the equilibrium chemistry retrieval (described in Section 4) using both 4 node (blue) and 6 node (red) Bézier spline P – T parametrization. The inset in, two corresponding colours, shows the best fit (solid line) and the 1σ bounds for the P – T, and the wavelength dependent $\tau(\lambda) = 2/3$ photosphere overplotted in the background. See Figure A1 for the cornerplot including all the free parameters in this retrieval.

the nodes themselves do not have bounded constraints as seen from their posteriors in Figure A2, the P – T profile itself is well constrained in the range of pressures we compute the emission spectrum using GENESIS. We find that both the free and equilibrium chemistry retrievals indicate a P – T profile which going from high to low pressures is non-inverted until around 0.1 bar, where it switches to become inverted.

To test how robust the shape of the P – T profile is, we ran retrievals with alternative parametrizations for the profile. This also checks how sensitive the constrained abundances are to the choice of P – T parametrization. We first tested a retrieval with 6 node Bézier profile for the equilibrium chemistry case, which after fixing the pressure

values for the nodes at the top and bottom of the pressure range, adds four more free parameters to the original 4 node Bézier profile. We find that both the retrieved P – T profile and the metallicity are consistent between 4 and 6 node Bézier spline parametrization (as shown in Figure 6 and discussed further in Appendix B). Going forward, we refer to the constraints from the 4 node Bézier profile in the context of equilibrium chemistry retrievals, unless specified otherwise.

We also ran two equilibrium chemistry retrievals using a simpler linear gradient P – T profile (as used in Panwar et al. (2024)), one forced to be only inverted and the other forced to be only non-inverted. The two profiles have a linear gradient in temperature with

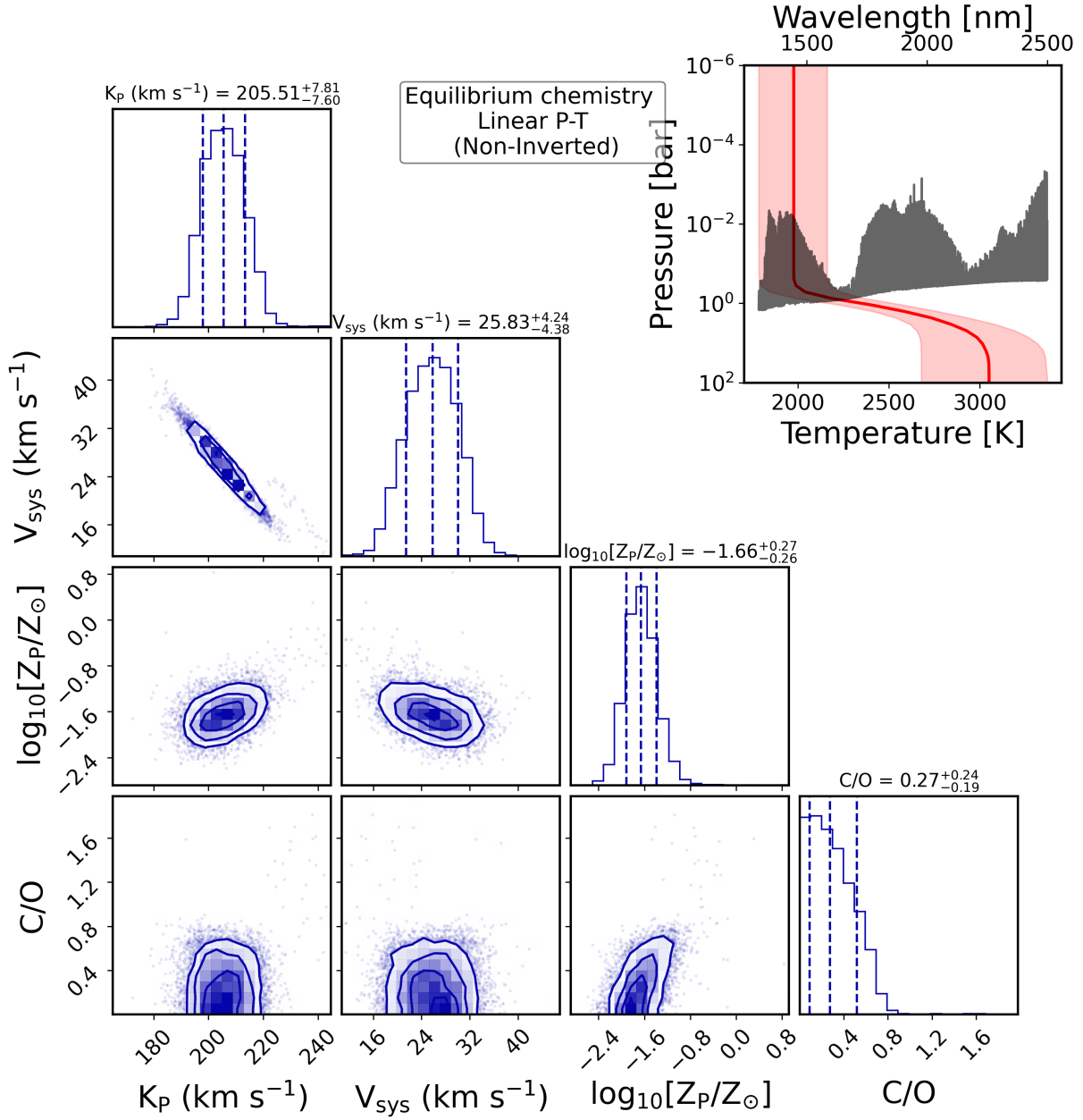


Figure 7. Same as Figure 6, but using a linear gradient P – T with no inversion.

respect to $\log(P)$ between two points in the atmosphere (four free parameters : P_1, T_1, P_2, T_2), and is isothermal otherwise. Comparing the Bayesian evidence from MultiNest for these two retrievals, we find that the non-inverted P – T profile is significantly preferred over the inverted one by $\Delta \ln Z = 9$. The retrieval with non-inverted profile converges to parameters consistent with the Bézier spline profile retrieval within 1σ , as shown in Figure 7, and Table 3. However, we also find that the $\Delta \ln Z$ between the non-inverted linear P – T profile and Bézier spline profile both 4 and 6 nodes is negligible, indicating that there is no strong preference for the switch to inversion indicated by the Bézier spline profile. We also confirm this by running another equilibrium chemistry retrieval using the P – T profile parametrization from Madhusudhan & Seager (2009), as shown and discussed in more detail in Appendix B. The P – T profiles obtained from dif-

ferent model parametrizations are shown for comparison in Figure 10.

We tested another retrieval case which included using a blackbody instead of the PHOENIX stellar photosphere model to compute F_S . We find that in both alternative retrieval setups, we obtain consistent P – T profiles, sub-solar atmospheric metallicities and solar/sub-solar C/O ratios, and sub-solar abundances of H₂O. Furthermore, we also ran a free chemistry retrieval ((Madhusudhan & Seager 2009) profile, H₂O and CO abundance free) keeping planetary rotational velocity ($v_p \sin i$) free. We find that even when keeping $v_p \sin i$ free, our constraints are robust against potential degeneracy between the molecular abundances and the broadening of spectral lines due to sources like atmospheric circulation or superrotation. The results from these alternative models, shown in Appendix B, C, and D, strengthen the robustness of our constraints on the atmosphere of

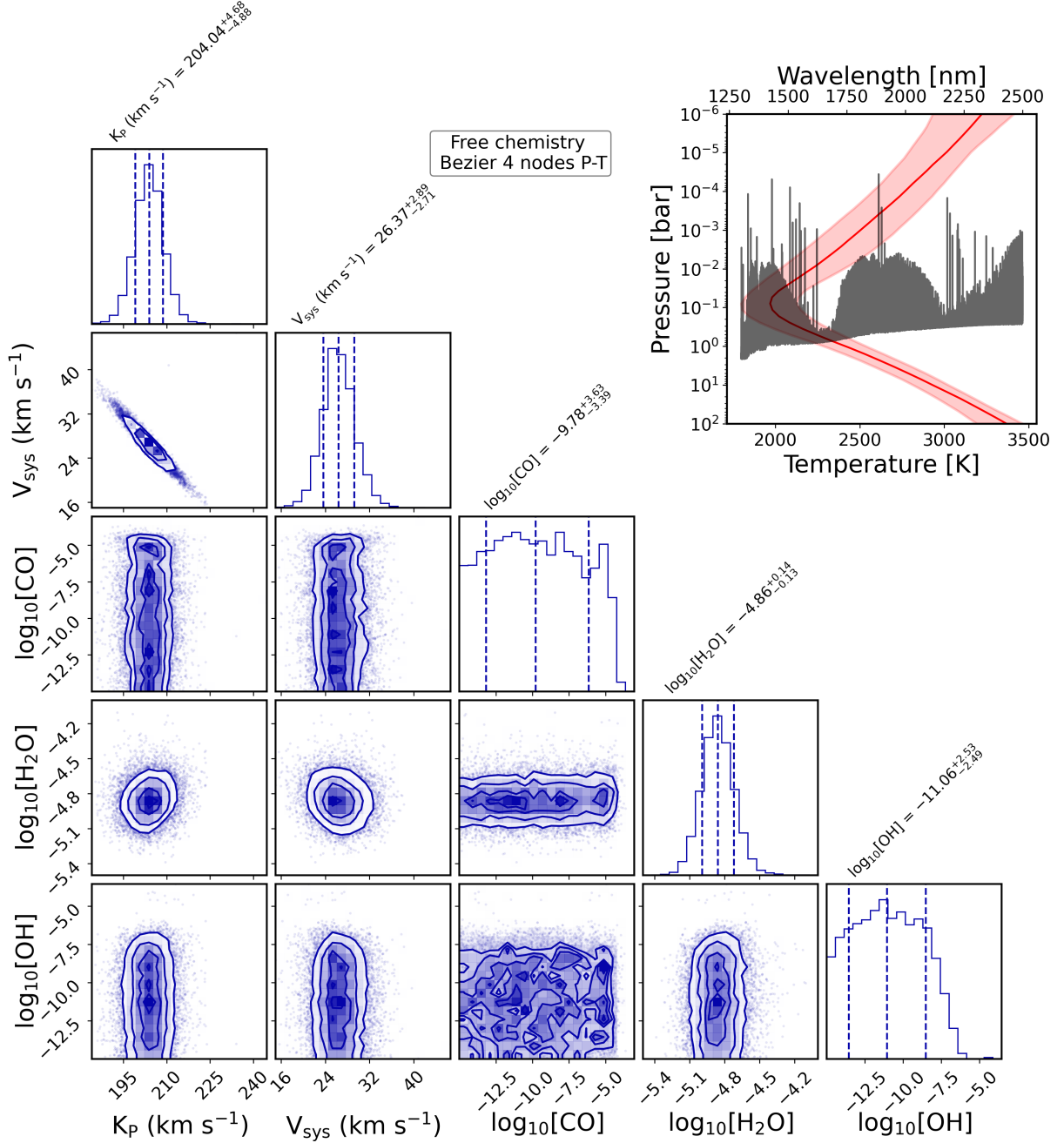


Figure 8. Same as Figure 6, but for the free-chemistry retrieval. Note that the H₂O abundance plotted here is the deep abundance of H₂O, and all species except H₂O in the free-chemistry retrieval are assumed to have vertically uniform abundance profile.

WASP-122b against a range of model assumptions. We discuss the constraints on WASP-122b’s thermal structure in the context of its sub-solar metallicity atmosphere in Section 5.1.

4.2 K_p - V_{sys} Cross-Correlation Map from the Retrieved Model

We measure $K_p = 204.91^{+7.37}_{-7.26}$ km s⁻¹ and $V_{\text{sys}} = 25.97^{+4.29}_{-4.22}$ km s⁻¹ from the equilibrium chemistry retrieval, which is consistent within 1σ with the values constrained by the free chemistry retrieval ($K_p = 204.08^{+4.74}_{-4.92}$ km s⁻¹ and $V_{\text{sys}} = 26.34^{+2.92}_{-2.74}$ km s⁻¹). The measured precision on the velocities is marginally lower than those from similar observations from IGRINS (e.g. Smith et al. (2024); Brogi et al.

(2023) due to the lack of post-eclipse data. The best-fit values for both K_p and V_{sys} are shifted from the expected literature values (listed in Table 1) by $\sim 3\sigma$, which could be a signature of atmospheric dynamics and inhomogeneity (e.g. Beltz et al. (2023); Wardenier et al. (2024, 2025)). We discuss this in more detail in Section 5.4.

Following the same steps as in Section 3, but using the best fit retrieved model instead of the 1D-RCTE model, we compute the K_p - V_{sys} map for the CCF S/N and the log-likelihood derived confidence intervals. The resulting CCF S/N map shows a peak centred at the K_p and V_{sys} constrained by the retrieval, with the S/N of the CCF peak as 3σ , obtained by subtracting the median of the CCF K_p - V_{sys} map and dividing by its standard deviation. We note that the

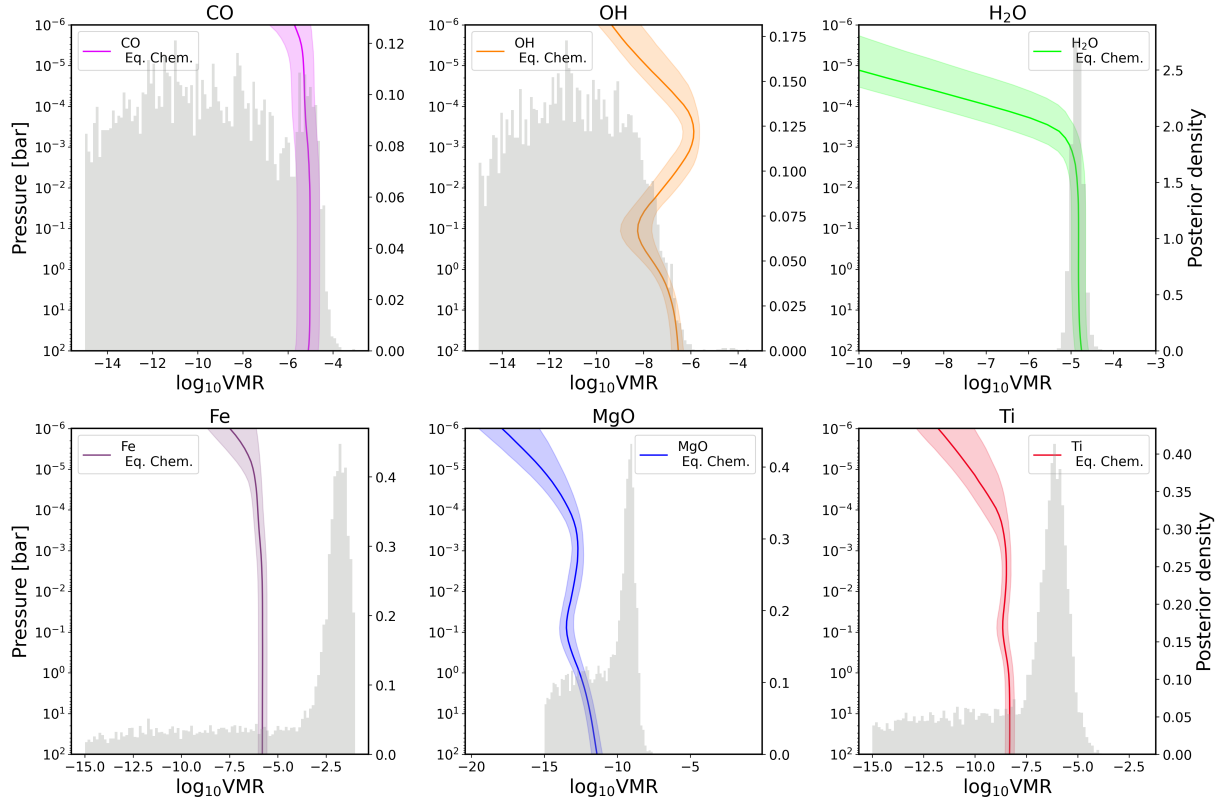


Figure 9. Vertical abundance profiles from the equilibrium chemistry retrieval, and posteriors for corresponding species from the free chemistry retrieval assuming vertically uniform abundances (except for H_2O , see Section 4.) By comparing the inferences for the molecular abundances from both equilibrium (which only has metallicity and C/O ratio as the free parameters deciding the abundance profiles at equilibrium) and free-chemistry posteriors, we conclude that H_2O is the only species for which the data yields a constraint with bounded posteriors. All the other species, despite having a peak in their posteriors, have a finite tail that fills up the retrieval prior, and hence only yield upper limits.

value of CCF S/N computed this way is not a very robust metric for the significance of detection, as it can be biased by the overall noise structure in the $K_P - V_{\text{sys}}$ map. A better, more statistically motivated approach, is to instead use the log-likelihood values derived from the CCF themselves, as done for the RCTE model in Section 3. We find that the signal in log-likelihood space is tightly constrained, with the corresponding $\pm 3\sigma$ confidence interval lying well within the $\pm 3\sigma$ of the best-fit K_P and V_{sys} measured from the retrievals.

We also checked for the contributions from individual molecular species in the model by following the same steps as Smith et al. (2024), which involves computing the difference between the $K_P - V_{\text{sys}}$ map corresponding to model with all the species and the $K_P - V_{\text{sys}}$ map for the same model but a given species removed. We find that the $K_P - V_{\text{sys}}$ map for H_2O shows a clear significant peak, but none of the other species in the model show a detection (as shown in Figure E1). This aligns with the unconstrained posteriors obtained from the free-chemistry retrievals for all species except H_2O , indicating that the detection is driven primarily by H_2O .

5 DISCUSSION

5.1 Metallicity and thermal structure of WASP-122b

Both free and equilibrium chemistry retrievals indicate that WASP-122b has an atmosphere with significantly sub-solar metallicity, and emission spectrum with lines in absorption rather than emission. We highlight that in the context of our retrieval constraints on the

metallicity and $P - T$ profile, the solar composition assumption for the 1D-RCTE model is incorrect. The solar composition 1D-RCTE model has all the spectral lines in emission in the IGRINS wavelength range. The wavelength dependent photosphere (the pressure at which the wavelength dependent optical depth $\tau(\lambda) = 2/3$) of the 1D-RCTE model is centred roughly around 0.001 bar. In contrast, the retrieved best-fit model with best-fit sub-solar metallicity $\log_{10}[\text{Z}_P/\text{Z}_\odot] = -1.48$ dex has most of the spectral lines in absorption (as shown in Figure 4), and its $\tau(\lambda) = 2/3$ photosphere is centred deeper in the atmosphere around 0.1 bar. This helps to explain the observed anti-correlation in the CCF $K_P - V_{\text{sys}}$ computed using the solar composition 1D-RCTE model, and a positive correlation with the best-fit retrieved model, as shown in Figure 4. Note that the pressures $P(\lambda)\tau = 2/3$ only simply indicate pressure levels from which most of the photons are emitted at a given wavelength. In reality, the total flux emitted at a given wavelength comes from a range of pressure levels, and this can be visualized through a contribution function as defined by Knutson et al. (2008), adapted from Equations 4.4.1 to 4.4.8 in Chamberlain & Hunten (1987) (for along the zenith, that is $\mu = \cos\theta = 1$):

$$cf(P, \lambda) = B(\lambda, T(P)) \frac{\Delta e^{-\tau(\lambda, P)}}{\Delta \log(P)} \quad (5)$$

where $B(\lambda, T(P))$ is the blackbody emission expected at a given wavelength λ and temperature $T(P)$ (at the given pressure level, defined by the $P - T$ profile), and $\tau(\lambda, P)$ is the optical depth at the given

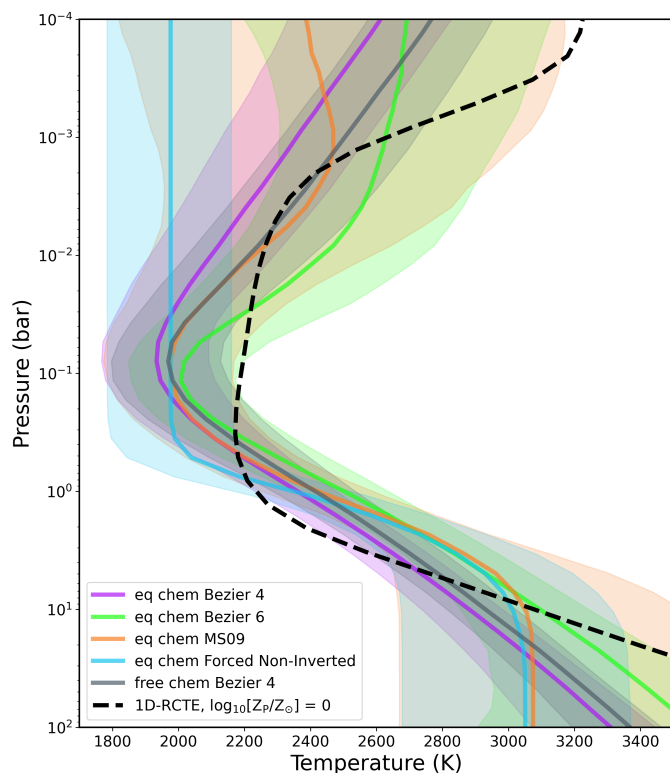


Figure 10. Comparison of the $P - T$ profiles constrained from a range model parametrizations, and from the 1D-RCTE model assuming solar metallicity (dashed black). The solid lines show the best fit $P - T$ profiles obtained from 5 different retrievals, one of which assumes free chemistry and uses the 4 node Bézier spline profile, and the other four of which assume equilibrium chemistry with a range of $P - T$ profile parametrizations: 4 node Bézier spline, 6 node Bézier spline, Madhusudhan & Seager (2009) (MS09) profile, and a forced non-inverted linear gradient profile. The shaded region for each profile represent the $\pm 1\sigma$ intervals indicated by the corresponding retrieval posteriors.

pressure and wavelength. This form of contribution function essentially represents the intensity from a given pressure layer, assuming a Planck source function. The $\tau(\lambda, P)$ is governed by both $P - T$ profile and the abundances of species with relatively high opacities in a given wavelength range. Following Equation 5, we computed the contribution function for three cases: 1) 1D-RCTE $P - T$ profile with $\log_{10}[Z_p/Z_\odot] = 0$ (solar composition), 2) 1D-RCTE $P - T$ profile with $\log_{10}[Z_p/Z_\odot] = -2$ dex, and 3) Retrieved $P - T$ profile with $\log_{10}[Z_p/Z_\odot] = -1.48$ dex. The contribution functions obtained for all three cases are shown in Figure 11.

We find that for the solar composition 1D-RCTE case, the contribution to the emission spectrum comes from a wide range of pressures spanning 1 to 0.001 bar. In contrast, for both the 1D-RCTE model with $\log_{10}[Z_p/Z_\odot]$ set to -2 dex, and -1.48 dex (best fit retrieved value), the contribution comes from a smaller range of pressures centred deeper in the atmosphere around 1 bar. This aligns with the intuitive expectation for an H/He dominated atmosphere like that of WASP-122b. Decreasing atmospheric metallicity leads to an average decrease in optical thickness across the wavelength range, which means that photons originating deeper in the atmosphere can still escape, with lesser chance of being absorbed as compared to the case of an atmosphere with higher optical thickness due to higher metallicity. The effect of decreasing metallicity on the self-consistently

computed RCTE thermal structure for WASP-122b can be seen for the metallicity set to -2 dex in the middle panel in Figure 11. In contrast to the solar composition case which is largely inverted in ~ 1 to 0.01 bar range, the $P - T$ profile for the sub-solar case is non-inverted in the same range of pressures. This change can be explained by the fact that decreasing metallicity leads to an overall decrease in molecular (TiO, VO, FeH) and atomic species (e.g. Fe, Mg, and Na) which cause thermal inversion by absorbing the bulk of incoming optical stellar irradiation. Note however that decreasing the metallicity from solar to -2 dex solar is not enough to remove the inversion in the upper atmosphere (pressures $< 10^{-3}$), where the inversion is driven by the onset of thermal dissociation of H_2O , which reduces the ability of the atmosphere to cool effectively by emitting radiation in the infrared.

As shown in Figure 11, a sub-solar metallicity atmosphere pushes the contribution function for the emission spectrum of WASP-122b deeper in the atmosphere (as compared to the RCTE solar metallicity model), around 1 bar, where the $P - T$ profile is non-inverted. This is true for all the alternative $P - T$ profile parametrizations we tested in Section 4.1. This explains why the RCTE model led to an anticorrelated peak in the $K_p - V_{\text{sys}}$ map, whereas the retrieved model yields a positive peak (as shown in Figure 4). The solar composition RCTE model has the contribution function spanning largely the inverted part of the $P - T$ profile, leading to nearly all spectral lines in emission. In contrast, the retrieved best fit model with sub-solar metallicity has the contribution function restricted largely to the non-inverted part of the $P - T$ profile, leading to the spectral lines emanating from the region around 1 bar to be in absorption. We note that since the contribution function for the best fit model is restricted to a narrow range in deep atmosphere, we obtain weaker constraint on the nature of the $P - T$ profile in the upper atmosphere (as discussed previously in Section 4.1). On inspecting the best fit emission spectrum model with its corresponding continuum set by the $H_2 - H_2$ and $H_2 - He$ collision induced absorption (CIA) (Figure 12, we indeed confirm that most of the spectral lines are in emission, and the weak constraint on the possible change to inversion in the $P - T$ profile in the upper atmosphere (pressures < 0.1 bar) comes from a very small number of lines in emission towards the reddest end of K band.

In the context of the overall population of hot and ultra-hot Jupiters, the $P - T$ profile constrained by our retrieval supports the idea that for equilibrium temperature similar to WASP-122b ($T_{\text{eq}} \sim 1900$ K), hot-Jupiters have possibly already begun transitioning from having non-inverted to inverted thermal structure in the upper atmosphere pressure ranges < 0.1 bar. However, our retrievals only obtain the tightest constraint on the $P - T$ profile in layers at pressure > 0.1 bar, and stronger constraints on the upper atmosphere (< 0.1 bar) are needed to confirm this transition. If confirmed, this would roughly agree with the results from Baxter et al. (2021) who analyzed a statistical sample of hot to ultra-hot Jupiter secondary eclipses observed using Spitzer 3.6 and $4.5 \mu\text{m}$ and find that the transition to inversions based on the emission from CO in the $4.5 \mu\text{m}$ channel happens around 1660 ± 100 K. Curiously, WASP-122b's metallicity of $0.033^{+0.018}_{-0.016} \times \text{solar}$ falls within the predicted range of metallicities (0.03 to $30 \times \text{solar}$) required to explain the scatter in the H_2O absorption features measured by HST/WFC3 for a sample of 19 hot and ultra-hot Jupiters Mansfield et al. (2021).

Our findings for WASP-122b highlight the fact that whether an inverted or non-inverted $P - T$ profile leads to spectral signatures in emission or absorption respectively depends on the atmospheric composition, which governs the range of pressures where the contribution function for the emission spectrum peaks. This is especially important for the high spectral resolution and wide wavelength range data,

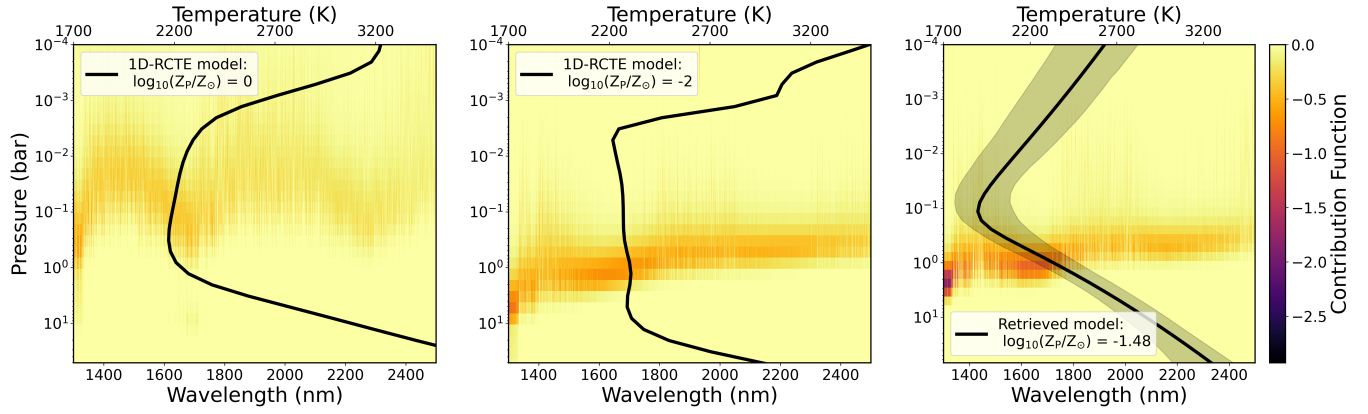


Figure 11. Wavelength dependent contribution functions for the combination of P – T profile (overplotted) and metallicity for WASP-122b across three cases: (Left panel) 1D-RCTE model P – T profile with solar metallicity, (Middle panel) 1D-RCTE model P – T profile with -2 dex solar metallicity, and (Third panel) Retrieved P – T profile from the equilibrium chemistry retrieval, with the corresponding retrieved best fit metallicity of -1.48 dex (shaded region showing the $\pm 1\sigma$ bounds obtained from the retrieved posteriors.). The darker regions in the map correspond to a higher contribution to the emission spectrum. Note that for the solar metallicity 1D-RCTE model, the contribution function spans a wide range of pressures from 1 to 0.001 bar, covering the inverted part of the P – T profile, whereas reducing the metallicity pushes the contribution function deeper in the atmosphere to a smaller range of pressures (10 to 1 bar), which for the case of the retrieved model leads to most of the spectral lines emanating from the deeper non-inverted part of the P – T profile causing them to be in absorption.

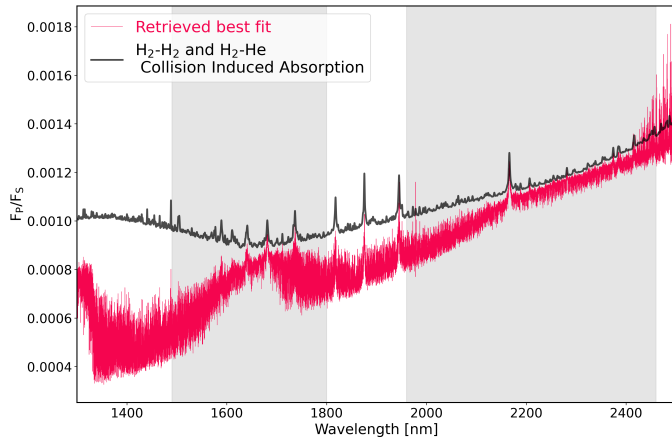


Figure 12. Best fit emission spectrum model for WASP-122b obtained from the equilibrium chemistry retrieval in comparison with its corresponding $\text{H}_2\text{-H}_2$ and $\text{H}_2\text{-He}$ collision induced absorption (CIA) contribution. The shaded region shows the H and K wavelength bands covered by the IGRINS observations in this work. The majority of the spectrum probed by our observations has absorption lines, except the reddest end of K band where there are a small number of lines in emission.

similar to the one presented in this work, which has adequate sensitivity to precisely constrain the line shapes and contrast. This was also indicated earlier by the high-resolution emission spectroscopy of HD 209458 b by Schwarz et al. (2015), albeit in a narrower wavelength of CRIRES (2.305 to 2.33 μm) as compared to IGRINS (1.45 to 2.42 μm). Schwarz et al. (2015) show that a model corresponding to a strongly inverted P – T profile results in an anti-correlated peak in the CCF $K_p - V_{\text{sys}}$ map similar to what we obtain for the 1D-RCTE profile, but a near-isothermal profile shows a positive peak, indicating the lack of strong thermal inversion on the day side of the planet. Schwarz et al. (2015) also note that a weakly inverted thermal profile yields spectral lines with their wings (probing the continuum) in absorption but the cores (probing lower pressures) in emission.

Similar complex behaviour of mixed absorption and emission features from H_2O and CO in the same spectrum (from 1.4 to 3.6 μm) due to the two species probing either inverted or non-inverted parts of the P – T profile was predicted by Parmentier et al. (2018) for WASP-121b, particularly relevant at high resolutions (see their Figure 8). We note, however, that the two recent works that have studied the atmosphere WASP-121b using IGRINS (Smith et al. 2024) and CRIRES+ and ESPRESSO (Pelletier et al. 2025) measure a dayside emission spectrum with all lines including CO and H_2O CRIRES+ and ESPRESSO wavelength range are in emission, indicating that the dayside of the planet has an inverted thermal structure and solar to slightly super-solar composition atmosphere.

In summary, high-resolution spectroscopy data with wide wavelength coverage have enough information that a model with adequate flexibility in chemical abundance and P – T profile parametrizations can indeed capture the complexity of the underlying chemical composition and thermal structure. In this context, we also emphasize the importance of moving beyond a simple dichotomy of inversion /non-inversion leading to spectral emission/ absorption lines when considering the emission spectra of hot and ultra-hot Jupiters. The better approach is to instead use model parametrizations with enough flexibility for atmospheric composition and P – T profile, which together govern the nature of atmospheric spectral signatures in high-resolution cross-correlation spectroscopy data.

5.2 Comparison with previous studies for WASP-122b

Stangret et al. (2024) conducted high-resolution spectroscopy of WASP-122b during its primary transit in the visible wavelength range using ESPRESSO, and found that the planet's orbit is aligned with the stellar spin axis (spin-orbit obliquity $\lambda = 0.09^{+0.88}_{-0.90}$ deg). Stangret et al. (2024) also conducted a search for a range of atomic and molecular species using cross-correlation, and found no evidence of absorption from any of the species, including H_2O . We compare our constraints on the dayside atmosphere of WASP-122b with the findings of Stangret et al. (2024) for the terminator of the planet. A caveat with such comparison is that observations by Stangret et al. (2024) cover visible band whereas our observations cover the near-infrared

bands. Moreover, a direct one to one comparison of spectroscopy in transmission and emission is not straightforward because of the differences in the pressure and temperature ranges probed by both.

The non-detection of refractory bearing species (e.g. Fe, Mg, Ti, TiO, VO) in the ESPRESSO visible band data at the planet’s terminator is consistent with our non-detections of these species on the planet’s dayside, both explained by the sub-solar metallicity of the planet. If these species are in trace amounts on their relatively hotter dayside of the planet, the cooler temperatures at the terminator are likely to cause them to condense and make them further undetectable. In the case of H₂O, the non-detection in ESPRESSO could potentially be explained by a combination of comparatively smaller number of spectral lines in the ESPRESSO wavelength range as compared to IGRINS and the sub-solar abundance of H₂O decreasing the strength of the lines. However, we emphasize that this is a qualitative explanation, and we encourage further exploration in the visible band with other instruments, in both transmission and emission, to test these hypotheses.

5.3 Implications for the formation history of WASP-122b

Metallicity measurements for exoplanets through H₂O abundance measurements using HST (Kreidberg et al. 2014; Welbanks et al. 2019) and through H₂O, CO, and refractory measurements through ground-based high-resolution spectroscopy (e.g. Line et al. 2021; Smith et al. 2024) indicate a departure from the decreasing metal enrichment with increasing planetary mass as observed in the solar system gas-giants (Bean et al. 2023; August et al. 2023), also see Figure 13). This suggests there is a diversity in possible formation pathways across the exoplanet population as compared to the solar system. Both equilibrium chemistry and free retrievals on the IGRINS data indicate that WASP-122b has a C/O ratio consistent with solar and metallicity $\log_{10}[Z_p/Z_\odot] = -1.48^{+0.25}_{-0.22}$ dex or $0.033^{+0.018}_{-0.016} \times$ solar. The metallicity of the host star measured by the discovery papers Rodriguez et al. (2016) and Turner et al. (2016) (through Fe/H ratio from the visible band spectrum collected for radial velocity measurements) is $\log_{10}(\text{Fe}/\text{H}) = 0.326 \pm 0.09$ and $\log_{10}(\text{Fe}/\text{H}) = 0.32 \pm 0.09$ respectively, indicating that the host star is $2.09 \pm 0.43 \times$ solar metal rich. This implies WASP-122b has $0.016 \pm 0.009 \times$ the stellar metallicity, indicating that the planet’s atmosphere is severely metal depleted relative to the host star. As shown in Figure 13, the level of metal depletion observed for WASP-122b is lowest among all the other hot gas-giant exoplanets for which precise constraints on atmospheric metallicity have been obtained so far.

WASP-122b is less massive as compared to WASP-77Ab (previously characterized using IGRINS Line et al. (2021)), but shows an order of magnitude more metal depletion as compared to the latter, which has also been found to have an atmosphere with solar C/O ratio and sub-solar/stellar metallicity (Line et al. 2021; August et al. 2023; Smith et al. 2023). Similar to WASP-77Ab however, WASP-122b’s metal depleted atmosphere with solar/sub-solar C/O ratio does not align with the broad predictions from standard core-accretion model of planet formation Pollack et al. (1996). A gas-giant that forms beyond the snow lines of C and O bearing molecules (H₂O, CO, CO₂) and migrates after the disk dissipates is likely to end up with an elevated C/O ratio (following the C/O ratio of the gas in the disk) and low-metallicity atmosphere. In contrast, a gas-giant forming within the disk and migrating through it is likely to end up with O enriched atmosphere from accreting planetesimals, leading to low C/O and high-metallicity atmosphere (Öberg et al. 2011; Madhusudhan et al. 2014; Khorshid et al. 2022). WASP-122b’s solar/sub-solar C/O ra-

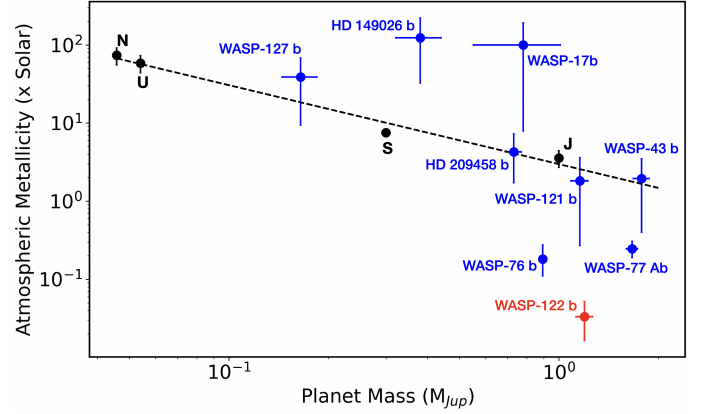


Figure 13. Atmospheric metallicity of WASP-122b constrained from IGRINS observations in this work in the planet mass vs atmospheric metallicity space along with solar system gas-giants and other gas-giant exoplanets with well constrained metallicity measurements. The values for the solar system gas-giants have been taken from Guillot et al. (2022) (using C/H as proxy for metallicity). Sources for other planets from HRCCS and emission spectroscopy, HST/WFC3, and JWST are: via (C+O)/H: WASP-77Ab (Smith et al. 2023), WASP-127b (Kanumalla et al. 2024), HD 149026b (Bean et al. 2023), HD 209458b (Xue et al. 2023), WASP-76b (Mansfield et al. 2024); via O/H: WASP-17b Gressier et al. (2025), WASP-43b Kreidberg et al. (2014); Bartelt et al. (2025); via (C+O+R)/H, where R is total abundance of refractory elements: WASP-121b Smith et al. (2024). A linear slope fit to the solar system values is shown in dashed line.

tio and sub-solar metallicity, similar to that of WASP-77 Ab, doesn’t align with either scenarios. Following the model predictions by Khorshid et al. (2023) for WASP-77 Ab, it is possible that WASP-122b could have formed beyond the CO or CO₂ snow line in a disk with part of the carbon budget locked in the soot phase, and migrated to a location beyond the H₂O snow line before the disk dissipation.

Our upper limit on the C/O ratio to be solar/sub-solar is based on the non-detection of CO by both free and equilibrium chemistry retrievals. We note that the star WASP-122 is G4 type star with $T_{\text{eff}} = 5802 \pm 95$ K, which implies the stellar spectrum is expected to have significant CO absorption lines in the IGRINS wavelength range (especially in the K band) which could potentially contaminate the planetary CO signal. Our observations are taken during phases covering the planetary orbit well before the start of the secondary eclipse, which means that there should be an adequate shift in velocity space between the stellar and planetary CO lines causing negligible bias to the cross-correlation signal. We defer a more detailed simulation of the impact of stellar residuals on the retrievals to a future study.

5.4 Interpreting the measured shifts in K_p and V_{sys}

Shifts in the peak velocity at which the planetary signal is measured as compared to the expected velocity from the known orbital parameters have been used as proxies for atmospheric dynamics in hot Jupiters (Beltz et al. 2021; Savel et al. 2023; Brogi et al. 2023; Smith et al. 2024; Wardenier et al. 2024). For both the best fit K_p and V_{sys} values from the retrievals (both free and equilibrium chemistry) we find that the measured planetary signal is shifted in velocity from the expected literature values. With respect to the expected K_p and V_{sys} values from Rodriguez et al. (2016), our equilibrium chemistry retrieval measures a positive $\Delta K_p = 17.1 \pm 8.1$ km s⁻¹, and negative V_{sys} with $\Delta V_{\text{sys}} = -8.75 \pm 4.5$ km s⁻¹. Note that K_p represents the rate of change

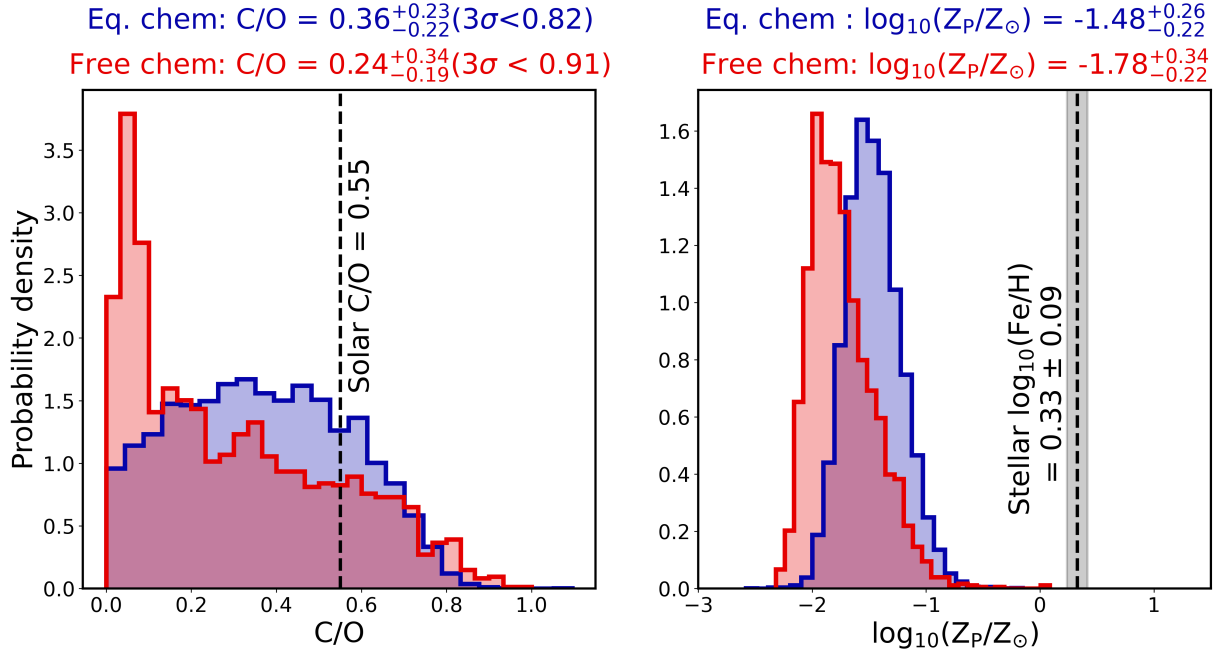


Figure 14. 1D posteriors for the C/O and metallicity of WASP-122b as compared to the solar and stellar values derived from the equilibrium chemistry retrieval (blue posteriors) and free chemistry retrieval (red posteriors).

of the Doppler shifts in the planet rest frame during the observation. The stronger the changes in Doppler shift in the planet rest frame, the larger the absolute value of ΔK_p . Wardenier et al. (2025) in their recently published GCM simulations find consistently negative ΔK_p driven by the planetary rotation. Negative ΔK_p implies that the line-of-sight velocities become less blueshifted (or more redshifted) in the planet rest frame over the course of the observation due to tidally locked rotation, and a larger part of the dayside rotating into view during pre-eclipse. The positive ΔK_p measured by us, and its absolute value much larger than the equatorial rotation velocity of WASP-122b (4.5 km s^{-1}), is in tension with the model predictions from Wardenier et al. (2025). The large magnitude of ΔV_{sys} , as compared to observed values of ΔV_{sys} e.g. $\sim 2 \text{ km s}^{-1}$ for the planet WASP-76b which has a similar equatorial rotational velocity (Wardenier et al. 2025), are also difficult to explain unless there are very strong winds, or an instrumental systematic effect.

It is worth noting here the relatively large uncertainties on both ΔK_p and ΔV_{sys} derived solely from pre-eclipse data in this work. Since we only have pre-eclipse data for the planet, our posteriors for K_p and V_{sys} are highly correlated and hence the measured precision for both is low. Further observations covering post-eclipse phases are needed to improve the precision on both K_p and V_{sys} to confirm these findings, and shed further light on the differences from model predictions.

6 CONCLUSIONS

In this work, we have presented high-resolution near-infrared emission spectroscopy observations of the hot-Jupiter WASP-122b, which occupies the transitional regime between hot to ultra-hot Jupiters. We used IGRINS on Gemini-South to observe the day-side of WASP-122b during pre-secondary eclipse orbital phases. Based on our analysis using established 1D HRCCS techniques, we conclude the fol-

lowing about the atmospheric chemical composition and thermal structure of the day-side of WASP-122b:

- We find that the solar composition 1D-RCTE model for WASP-122b, which predicts an inverted $P - T$ profile with all spectral lines in emission, yields an anti-correlated peak in the cross-correlation map close to the expected K_p and V_{sys} for the system. This indicates that the planetary signal in the data has lines largely in absorption rather than all in emission.
- Using a suite of retrievals with varying prescriptions for the chemistry (free and equilibrium), $P - T$ profile parametrizations (Bézier spline and Madhusudhan & Seager (2009)) and stellar spectrum (using PHOENIX and Blackbody), we find that WASP-122b has an atmosphere with significantly sub-solar metallicity $\log_{10}[Z_p/Z_{\odot}] = -1.48^{+0.25}_{-0.22}$ dex, solar/sub-solar C/O ratio (3σ upper limit 0.82), and a non-inverted $P - T$ profile. The measured sub-solar atmospheric metallicity is primarily driven by the cross-correlation signal from H_2O . We do not find significant contribution to the cross-correlation signal from any other molecular or atomic species.
- We find that the sub-solar metallicity of WASP-122b pushes the contribution function for the emission spectrum in the IGRINS wavelength range to a relatively smaller range of pressures, deeper in the atmosphere (as compared to the solar composition 1D-RCTE model) around 1 bar where the $P - T$ profile is non-inverted. This leads to the H_2O spectral lines to be largely in absorption. Due to lack of contribution from upper layers of the atmosphere (pressures $< 10^{-1}$ bars) for the retrieved best fit model, we do not obtain a strong constraint on the nature of thermal profile in that region.
- The sub-solar metallicity of WASP-122b constrained from the IGRINS observations is lowest among all gas-giant exoplanets with well constrained atmospheric metallicity so far. This combined with the solar/sub-solar C/O ratio makes WASP-122b inconsistent with the predictions from standard core-accretion model, and alternative scenarios are needed to explain its formation history. It is possible that WASP-122b formed beyond the CO/CO_2 snow line in a disk with

part of the Carbon locked up in soot phase and migrated just beyond H_2O snow line before disk-dissipation.

- We find that the positive ΔK_p and the large magnitude of ΔV_{sys} constrained by us are inconsistent with the predictions from GCMs and typical expectation from planetary rotation respectively. However, due to the relatively large uncertainties on both measurements, further observations especially those covering post eclipse phases are needed to further investigate this inconsistency.

In light of our main result in this work about interplay of atmospheric composition and $P - T$ profile on the apparent spectra of hot-Jupiters, we highlight some final points relevant for WASP-122b, and in general for the future work on comparative studies of the hot and ultra-hot Jupiter population. Due to the limited orbital phase coverage of our observations (only pre-secondary eclipse), and relatively modest strength of the planetary signal in the data, we did not attempt to perform phase-resolved analyses to measure effects arising from spatially varying atmospheric composition and thermal structure from day to the night side of the planet. However, as recent works (Beltz et al. 2021; van Sluijs et al. 2023; Wardenier et al. 2024, 2025) have shown, the information content of HRCCS datasets are rich enough that with appropriate phase coverage and phase-resolved retrieval frameworks, these 3D variations in temperature, chemistry, and dynamics can indeed be measured through velocity shifts for individual chemical species. To probe these effects and obtain a more complete understanding of the role of 3D atmospheric properties on the apparent spectra, we recommend further observations of WASP-122b, covering the post-eclipse phases and transit in the near-infrared and visible band. These could also further provide insight into the positive ΔK_p and large ΔV_{sys} measured by us in this work.

Finally, we emphasize that our results for WASP-122b in this work join the continuing efforts for detailed atmospheric characterization and comparative studies of hot and ultra-hot Jupiters. In this context, the high sensitivity to line-shapes and contrasts provided by the powerful combination of wide wavelength coverage (similar to IGRINS), high spectral resolution, and flexible retrieval model parametrizations, can play a crucial in measuring the complexities in temperature and compositional profiles and the various thermochemical mechanisms that affect them across the population of irradiated gas-giant exoplanets.

ACKNOWLEDGEMENTS

We thank Luke Parker, Jayne Birkby, Anjali Piette, Spandan Dash, and Lennart van Sluijs for insightful discussions related to this work. Vatsal Panwar and Heather Cegla acknowledge support from the UKRI Future Leaders Fellowship grant (MR/S035214/1, MR/Y011759/1). Vatsal Panwar also acknowledges support from the UKRI Science and Technology Facilities Council (STFC) through the consolidated grant ST/X001121/1. M.R.L. and K.K. acknowledge support from NSF grant AST-2307177. J.P.W. acknowledges support from the Canadian Space Agency (CSA) [24JWGO3A-03] and the Trottier Family Foundation via the Trottier Postdoctoral Fellowship held at the Institute for Research on Exoplanets (IREx). M.W.M. acknowledges support from the Heising-Simons Foundation through the 51 Pegasi b Fellowship program. P.C.B.S. acknowledges support provided by NASA through the NASA FINESST grant 80NSSC22K1598. This work is based on observations obtained at the international Gemini Observatory, a program of NSF's NOIRLab, which is managed by the Association of Universities for Research in Astronomy (AURA) under a cooperative agreement with the National Science Foundation on behalf of the Gemini Observatory part-

nership: the National Science Foundation (United States), National Research Council (Canada), Agencia Nacional de Investigación y Desarrollo (Chile), Ministerio de Ciencia, Tecnología e Innovación (Argentina), Ministério da Ciência, Tecnologia, Inovações e Comunicações (Brazil), and Korea Astronomy and Space Science Institute (Republic of Korea). This work used the Immersion Grating Infrared Spectrometer (IGRINS) that was developed under a collaboration between the University of Texas at Austin and the Korea Astronomy and Space Science Institute (KASI) with the financial support of the US National Science Foundation 27 under grants AST-1229522 and AST-1702267, of the University of Texas at Austin, and of the Korean GMT Project of KASI. This work used open source software packages that include matplotlib (Hunter 2007), numpy (Harris et al. 2020), pymultinest (Buchner et al. 2014), and scipy (Virtanen et al. 2020).

DATA AVAILABILITY

The raw science data included in this work are publicly available on the Gemini Observatory archive. The processed data, analysis outputs, and the code used to make the figures in the paper are available at <https://doi.org/10.5281/zenodo.15847396>.

REFERENCES

- Arcangeli J., et al., 2018, *The Astrophysical Journal*, 855, L30
 Asplund M., Amarsi A. M., Grevesse N., 2021, *Astronomy and Astrophysics*, 653, A141
 August P. C., Bean J. L., Zhang M., Lunine J., Xue Q., Line M., Smith P. C. B., 2023, *The Astrophysical Journal*, 953, L24
 Barman T. S., Hauschildt P. H., Allard F., 2005, *The Astrophysical Journal*, 632, 1132
 Bartelt D., et al., 2025, *The Astronomical Journal*, 169, 101
 Baxter C., et al., 2020, *Astronomy and Astrophysics*, 639, A36
 Baxter C., et al., 2021, *Astronomy & Astrophysics*, 648, A127
 Bean J. L., et al., 2023, *Nature*, 618, 43
 Beltz H., Rauscher E., Brogi M., Kempton E. M.-R., 2021, *The Astronomical Journal*, 161, 1
 Beltz H., Rauscher E., Kempton E., Malsky I., Savel A., 2023, Magnetic Effects and 3D Structure in Theoretical High-Resolution Transmission Spectra of Ultrahot Jupiters: the Case of WASP-76b, <http://arxiv.org/abs/2302.13969>
 Bernath P. F., 2020, *Journal of Quantitative Spectroscopy and Radiative Transfer*, 240, 106687
 Birkby J. L., 2018, Exoplanet Atmospheres at High Spectral Resolution, <http://arxiv.org/abs/1806.04617>
 Birkby J. L., de Kok R. J., Brogi M., de Mooij E. J. W., Schwarz H., Albrecht S., Snellen I. A. G., 2013, *Monthly Notices of the Royal Astronomical Society*, 436, L35
 Brogi M., Line M. R., 2019, *The Astronomical Journal*, 157, 114
 Brogi M., Snellen I. A. G., de Kok R. J., Albrecht S., Birkby J., de Mooij E. J. W., 2012, *Nature*, 486, 502
 Brogi M., Line M., Bean J., Désert J. M., Schwarz H., 2017, *The Astrophysical Journal*, 839, L2
 Brogi M., et al., 2023, *The Astronomical Journal*, 165, 91
 Buchner J., et al., 2014, *Astronomy & Astrophysics*, 564, A125
 Buldyreva J., Yurchenko S. N., Tennyson J., 2022, *RAS Techniques and Instruments*, 1, 43
 Burrows A., Hubeny I., Budaj J., Knutson H. A., Charbonneau D., 2007, *The Astrophysical Journal*, 668, L171
 Chamberlain J. W., Hunten D. M., 1987, Theory of planetary atmospheres. An introduction to their physics and chemistry.. Vol. 36
 Chevallier C. J., Madhusudhan N., Holmberg M., 2023, *Monthly Notices of the Royal Astronomical Society*, 522, 661

- De Kok R., Brogi M., Snellen I., Birkby J., Albrecht S., De Mooij E., 2013, *Astronomy & Astrophysics*, 554, A82
- Deibert E. K., et al., 2024, *The Astronomical Journal*, 168, 148
- Feroz F., Hobson M. P., Bridges M., 2009, *Monthly Notices of the Royal Astronomical Society*, 398, 1601
- Fortney J. J., Saumon D., Marley M. S., Lodders K., Freedman R. S., 2006, *The Astrophysical Journal*, 642, 495
- Fortney J. J., Lodders K., Marley M. S., Freedman R. S., 2008, *The Astrophysical Journal*, 678, 1419
- Gandhi S., Madhusudhan N., 2017, *Monthly Notices of the Royal Astronomical Society*, 472, 2334
- Gandhi S., Kesseli A., Snellen I., Brogi M., Wardenier J. P., Parmentier V., Welbanks L., Savel A. B., 2022, *Monthly Notices of the Royal Astronomical Society*, 515, 749
- Garhart E., et al., 2020, *The Astronomical Journal*, 159, 137
- Gibson N. P., et al., 2020, *Monthly Notices of the Royal Astronomical Society*, 493, 2215
- Gressier A., et al., 2025, *The Astronomical Journal*, 169, 57
- Griffith C. A., Yelle R. V., Marley M. S., 1998, *Science*, 282, 2063
- Guillot T., Fletcher L. N., Helled R., Ikoma M., Line M. R., Parmentier V., 2022, Giant Planets from the Inside-Out, doi:10.48550/arXiv.2205.04100, <http://arxiv.org/abs/2205.04100>
- Harris C. R., et al., 2020, *Nature*, 585, 357
- Huang X., Freedman R. S., Tashkun S. A., Schwenke D. W., Lee T. J., 2013, *Journal of Quantitative Spectroscopy and Radiative Transfer*, 130, 134
- Huang X., Schwenke D. W., Freedman R. S., Lee T. J., 2017, *Journal of Quantitative Spectroscopy and Radiative Transfer*, 203, 224
- Hubeny I., Burrows A., Sudarsky D., 2003, *The Astrophysical Journal*, 594, 1011
- Hunter J. D., 2007, *Computing in Science and Engineering*, 9, 90
- Husser T. O., Wende-von Berg S., Dreizler S., Homeier D., Reiners A., Barman T., Hauschildt P. H., 2013, *Astronomy and Astrophysics*, 553, A6
- Kanumalla K., et al., 2024, *The Astronomical Journal*, 168, 201
- Khorshid N., Min M., Désert J. M., Woitke P., Dominik C., 2022, *Astronomy & Astrophysics*, 667, A147
- Khorshid N., Min M., Désert J. M., 2023, *Astronomy & Astrophysics*, 675, A95
- Knutson H. A., et al., 2008, *The Astrophysical Journal*, 690, 822
- Kokori A., et al., 2023, *The Astrophysical Journal Supplement Series*, 265, 4
- Kreidberg L., et al., 2014, *The Astrophysical Journal*, 793, L27
- Kreidberg L., et al., 2018, *The Astronomical Journal*, 156, 17
- Kurucz R. L., 2018, p. 47, <https://ui.adsabs.harvard.edu/abs/2018ASPC...515...47K>
- Lee J.-J., Gullikson K., 2016, *Zenodo*
- Li G., Gordon I. E., Rothman L. S., Tan Y., Hu S.-M., Kass S., Campargue A., Medvedev E. S., 2015, *The Astrophysical Journal Supplement Series*, 216, 15
- Line M. R., et al., 2013, *The Astrophysical Journal*, 775, 137
- Line M. R., et al., 2021, *Nature*, 598, 580
- Lothringer J. D., Barman T., 2019, *The Astrophysical Journal*, 876, 69
- Mace G., et al., 2018, in Evans C. J., Simard L., Takami H., eds, Society of Photo-Optical Instrumentation Engineers (SPIE) Conference Series Vol. 10702, Ground-based and Airborne Instrumentation for Astronomy VII. p. 107020Q, doi:10.1117/12.2312345
- Madhusudhan N., Seager S., 2009, *The Astrophysical Journal*, 707, 24
- Madhusudhan N., Amin M. A., Kennedy G. M., 2014, *The Astrophysical Journal Letters*, 794, L12
- Mansfield M., et al., 2018, *The Astronomical Journal*, 156, 10
- Mansfield M., et al., 2021, *Nature Astronomy*, 5, 1224
- Mansfield M. W., et al., 2024, The metallicity and carbon-to-oxygen ratio of the ultra-hot Jupiter WASP-76b from Gemini-S/IGRINS, doi:10.48550/arXiv.2405.09769, <http://arxiv.org/abs/2405.09769>
- Marley M. S., Robinson T. D., 2015, *Annual Review of Astronomy and Astrophysics*, 53, 279
- McKemmish L. K., Masseron T., Hoeijmakers H. J., Pérez-Mesa V., Grimm S. L., Yurchenko S. N., Tennyson J., 2019, *Monthly Notices of the Royal Astronomical Society*, 488, 2836
- Mikal-Evans T., et al., 2022, *Nature Astronomy*, 6, 471
- Panwar V., Brogi M., Gandhi S., Cegla H., Lafarga M., 2024, The mystery of water in the atmosphere of tau Bootis b continues: insights from revisiting archival CRIRES observations, doi:10.48550/arXiv.2410.08178, <http://arxiv.org/abs/2410.08178>
- Parmentier V., et al., 2018, *A&A*, 617, A110
- Parmentier V., Showman A. P., Fortney J. J., 2021, *Monthly Notices of the Royal Astronomical Society*, 501, 78
- Pelletier S., et al., 2021, *The Astronomical Journal*, 162, 73
- Pelletier S., et al., 2023, *Nature*, 619, 491
- Pelletier S., et al., 2024, CRIRES+ and ESPRESSO reveal an atmosphere enriched in volatiles relative to refractories on the ultra-hot Jupiter WASP-121b, doi:10.48550/arXiv.2410.18183, <http://arxiv.org/abs/2410.18183>
- Pelletier S., et al., 2025, *The Astronomical Journal*, 169, 10
- Pinhas A., Madhusudhan N., Gandhi S., MacDonald R., 2019, *Monthly Notices of the Royal Astronomical Society*, 482, 1485
- Pino L., et al., 2020, *The Astrophysical Journal Letters*, 894, L27
- Piskorz D., et al., 2018, *The Astronomical Journal*, 156, 133
- Pollack J. B., Hubickyj O., Bodenheimer P., Lissauer J. J., Podolak M., Greenzweig Y., 1996, *Icarus*, 124, 62
- Polyansky O. L., Kyuberis A. A., Zobov N. F., Tennyson J., Yurchenko S. N., Lodi L., 2018, *Monthly Notices of the Royal Astronomical Society*, 480, 2597
- Prinath B., et al., 2022, *Nature Astronomy*, 6, 449
- Rodriguez J. E., et al., 2016, *The Astronomical Journal*, 151, 138
- Roth A., Parmentier V., Hammond M., 2024, *Monthly Notices of the Royal Astronomical Society*, 531, 1056
- Rothman L. S., et al., 2010, *Journal of Quantitative Spectroscopy and Radiative Transfer*, 111, 2139
- Savel A. B., Kempton E. M. R., Rauscher E., Komacek T. D., Bean J. L., Malik M., Malsky I., 2023, Technical report, Diagnosing limb asymmetries in hot and ultra-hot Jupiters with high-resolution transmission spectroscopy, <https://ui.adsabs.harvard.edu/abs/2023arXiv230101694S>, doi:10.48550/arXiv.2301.01694, <https://ui.adsabs.harvard.edu/abs/2023arXiv230101694S>
- Schwarz H., Brogi M., de Kok R., Birkby J., Snellen I., 2015, *Astronomy & Astrophysics*, 576, A111
- Seager S., Sasselov D. D., 1998, *The Astrophysical Journal*, 502, L157
- Smith P., et al., 2023, A Combined Ground-based and JWST Atmospheric Retrieval Analysis: Both IGRINS and NIRSpec Agree The Atmosphere of WASP-77A b is Metal-Poor, doi:10.48550/arXiv.2312.13069, <http://arxiv.org/abs/2312.13069>
- Smith P. C. B., et al., 2024, *The Astronomical Journal*, 168, 293
- Snellen I. A. G., de Kok R. J., de Mooij E. J. W., Albrecht S., 2010, *Nature*, 465, 1049
- Stangret M., et al., 2024, The obliquity and atmosphere of the hot Jupiter WASP-122b (KELT-14b) with ESPRESSO: An aligned orbit and no sign of atomic or molecular absorption, doi:10.48550/arXiv.2410.00800, <http://arxiv.org/abs/2410.00800>
- Stock J. W., Kitzmann D., Patzer A. B. C., Sedlmayr E., 2018, *Monthly Notices of the Royal Astronomical Society*
- Stock J. W., Kitzmann D., Patzer A. B. C., 2022, *Monthly Notices of the Royal Astronomical Society*, 517, 4070
- Sudarsky D., Burrows A., Hubeny I., 2003, *The Astrophysical Journal*, 588, 1121
- Turner O. D., et al., 2016, *Publications of the Astronomical Society of the Pacific*, 128, 064401
- Virtanen P., et al., 2020, *Nature Methods*, 17, 261
- Wardenier J. P., et al., 2024, Phase-resolving the absorption signatures of water and carbon monoxide in the atmosphere of the ultra-hot Jupiter WASP-121b with GEMINI-S/IGRINS, <http://arxiv.org/abs/2406.09641>
- Wardenier J. P., Parmentier V., Lee E. K. H., Line M. R., 2025, From pre-transit to post-eclipse: investigating the impact of 3D temperature, chemistry, and dynamics on high-resolution emission spectra of

the ultra-hot Jupiter WASP-76b, doi:10.48550/arXiv.2502.01606, <http://arxiv.org/abs/2502.01606>

Weiner Mansfield M., et al., 2024, *The Astronomical Journal*, 168, 14

Welbanks L., Madhusudhan N., Allard N. F., Hubeny I., Spiegelman F., Leininger T., 2019, *The Astrophysical Journal*, 887, L20

Xue Q., Bean J. L., Zhang M., Welbanks L., Lunine J., August P., 2023, JWST transmission spectroscopy of HD 209458b: a super-solar metallicity, a very low C/O, and no evidence of CH₄, HCN, or C₂H₂, doi:10.48550/arXiv.2310.03245, <http://arxiv.org/abs/2310.03245>

van Sluijs L., et al., 2023, *Monthly Notices of the Royal Astronomical Society*, 522, 2145

Öberg K. I., Murray-Clay R., Bergin E. A., 2011, *The Astrophysical Journal*, 743, L16

APPENDIX A: FULL POSTERIORIS FROM THE EQUILIBRIUM CHEMISTRY AND FREE CHEMISTRY RETRIEVALS

In this section, we show the full posterior distributions obtained from our retrievals assuming free chemistry and equilibrium (assuming 4 nodes Bézier spline P – T profile) as described in Section 4. Figure A1 and A2 show the cornerplots for all the free parameters in the equilibrium and free chemistry retrievals respectively.

APPENDIX B: TESTING THE EFFECT OF ALTERNATIVE P – T PROFILE PARAMETRIZATIONS

To test the robustness of our retrieval results against the choice of P – T profile parametrization, we performed an equilibrium chemistry retrieval with identical setup as described in Section 4, but with three alternative P – T profile parametrizations: 1) 6 nodes Bézier spline profile, 2) Linear P – T with no inversion, and 3) the 6 parameter prescription introduced by Madhusudhan & Seager (2009). The full posteriors from 1) are shown in Figure B1, from 2) in Figure B2, and from 3) in B3. The best fit parameters and their uncertainties are shown in Tables B1, 3, and B2 respectively.

In summary, the best fit parameters for the K_P , V_{sys} , C/O ratio, and metallicity ($\log_{10}[Z_P/Z_\odot]$) from all the alternative parametrizations are consistent with the equilibrium chemistry retrieval which uses the 4 node Bézier spline P – T parametrization. All the profiles follow the same non-inverted gradient in the same pressure ranges (0.1 to 1 bar) as the 4 node Bézier profile. However, in the upper atmosphere (<0.1 bar), all three alternative profiles are nearly isothermal and show a weaker inversion than the 4 node Bézier profile. This indicates that the constraint from the data on the thermal structure, regardless of the P – T parametrization, are the tightest in the high pressures ranging from 0.1 to 1 bar. This is consistent with the sub-solar metallicity consistently obtained from all the P – T parametrizations tested.

APPENDIX C: TESTING THE EFFECT OF COMPUTING F_S ASSUMING BLACKBODY RADIATION INSTEAD OF PHOENIX STELLAR MODEL

Since the host star WASP-122 is a G4 spectral type, the stellar spectrum F_S is expected to have CO lines with non-negligible depths, which means the choice of how we consider for F_S when computing F_P/F_S could potentially bias the retrieval when searching for CO in the planetary spectrum. To test our robustness against the choice of F_S , we repeated the equilibrium chemistry retrieval with the same setup as described in Section 4, but with F_S calculated as a blackbody

Table B1. Best fit and 1σ values for the parameters from equilibrium chemistry retrieval using the 6 node Bézier spline P – T profile parametrization.

K_P (km s ⁻¹)	[160.00, 250.00]	201.31 ^{+8.45} _{-5.10}
V_{sys} (km s ⁻¹)	[5.00, 50.00]	28.00 ^{+3.02} _{-5.14}
T_0 [K]	[400.00, 4500.00]	3548.80 ^{+296.66} _{-658.11}
T_1 [K]	[400.00, 4500.00]	1923.14 ^{+1576.35} _{-1032.37}
$\log_{10}P_1$ [bar]	[-6.00, 2.00]	-1.85 ^{+1.81} _{-1.28}
T_2 [K]	[400.00, 4500.00]	1314.07 ^{+814.67} _{-605.41}
$\log_{10}P_2$ [bar]	[-6.00, 2.00]	-0.08 ^{+1.32} _{-1.55}
T_3 [K]	[400.00, 4500.00]	2177.19 ^{+1447.29} _{-1155.19}
$\log_{10}P_3$ [bar]	[-6.00, 2.00]	-1.49 ^{+2.01} _{-1.98}
T_4 [K]	[400.00, 4500.00]	3232.03 ^{+791.52} _{-1075.56}
$\log_{10}P_4$ [bar]	[-6.00, 2.00]	-1.62 ^{+2.25} _{-2.54}
T_5 [K]	[400.00, 4500.00]	2530.93 ^{+957.25} _{-1175.21}
$\log_{10}[Z_P/Z_\odot]$	[-6.00, 2.00]	-1.72 ^{+0.21} _{-0.19}
C/O	[0.00, 2.00]	0.27 ^{+0.20} _{-0.17}

Table B2. Best fit and 1σ values for the parameters from equilibrium chemistry retrieval using the Madhusudhan & Seager (2009) P – T profile parametrization.

Parameter	Prior Bounds	Best-fit $\pm 1\sigma$
K_P (km s ⁻¹)	[160.00, 250.00]	203.71 ^{+7.42} _{-6.56}
V_{sys} (km s ⁻¹)	[10.00, 50.00]	26.69 ^{+3.76} _{-4.28}
T_{set} [K]	[1000.00, 3500.00]	2455.71 ^{+174.17} _{-179.08}
α_1	[0.02, 1.00]	0.68 ^{+0.23} _{-0.33}
α_2	[0.02, 1.00]	0.12 ^{+0.05} _{-0.02}
$\log_{10}P_1$ [bar]	[-6.00, 2.00]	-2.22 ^{+1.84} _{-0.78}
$\log_{10}P_2$ [bar]	[-6.00, 2.00]	-1.10 ^{+0.18} _{-1.57}
$\log_{10}P_3$ [bar]	[-6.00, 2.00]	0.58 ^{+0.44} _{-0.40}
$\log_{10}[Z_P/Z_\odot]$	[-6.00, 2.00]	-1.68 ^{+0.26} _{-0.23}
C/O	[0.00, 2.00]	0.25 ^{+0.23} _{-0.17}

spectrum corresponding to the stellar $T_{\text{eff}} = 5802$ K. The posteriors from this retrieval and the best fit parameters with their $\pm 1\sigma$ uncertainties are shown in Figure C1 and Table C1 respectively. In summary, the choice of whether we compute F_S using a PHOENIX model or assuming blackbody emission, does not affect our retrieved constraints on the C/O ratio, metallicity, and the P – T profile.

APPENDIX D: TESTING THE EFFECT OF FITTING FOR PLANETARY ROTATIONAL VELOCITY

The precise estimation of absolute abundance of species like H₂O depends heavily on the ability of the retrievals to fit the exact line profile. However, it is possible that there is a degeneracy between the abundance of water and the broadening of lines due to other sources like atmospheric circulation or superradiation, and that the inferred low abundance of H₂O might be a compensating factor for extra broadening of lines from these effects. To test this, we ran a free chemistry retrieval with H₂O and CO abundance as free parameters, using (Madhusudhan & Seager 2009) profile, and also keeping $v_P \sin i$ of the planet (which broadens the spectral lines) as a free parameter. We find that the constrained abundance of water remains unchanged even when allowing $v_P \sin i$ to be free. The posteriors from this

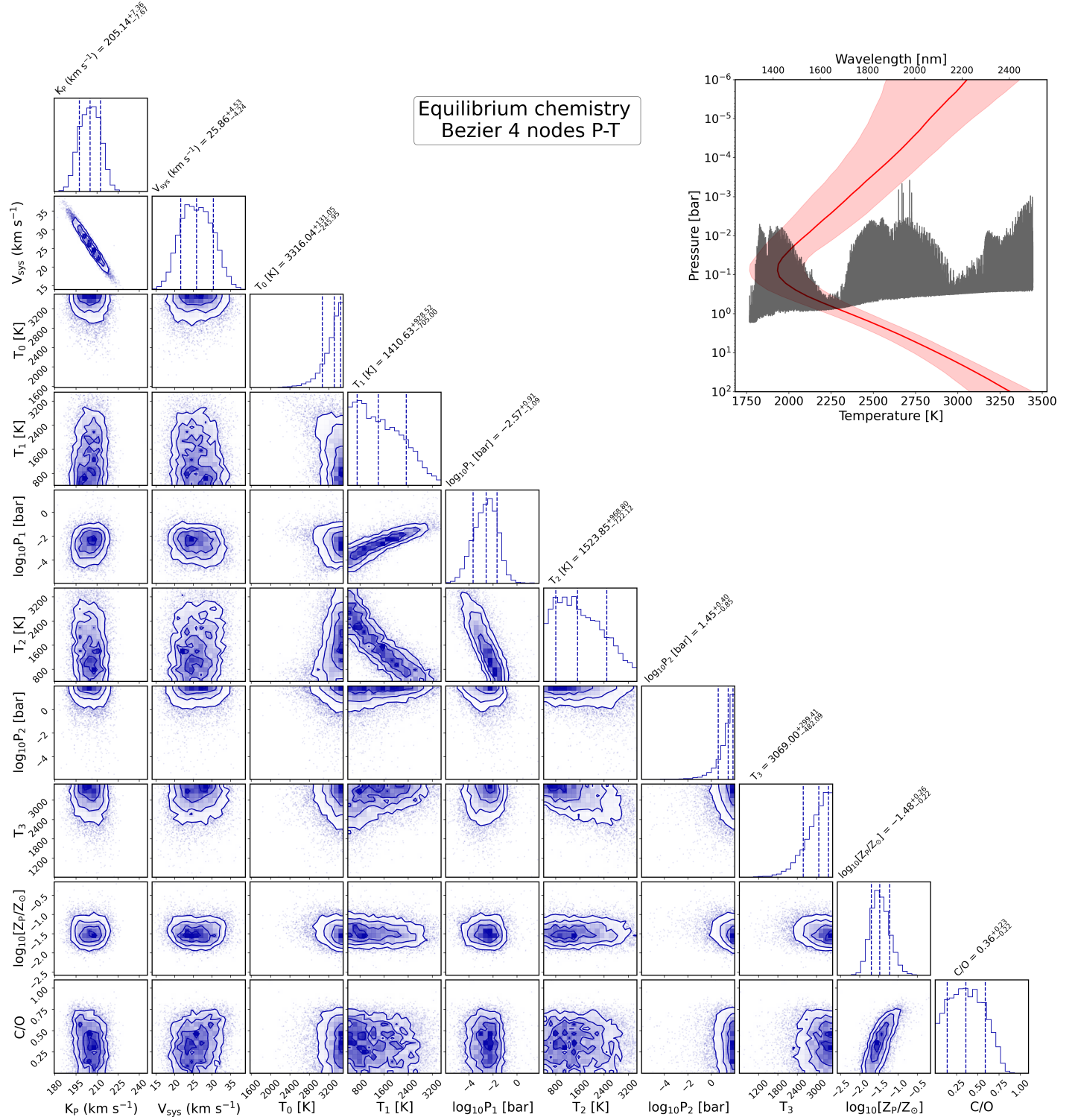


Figure A1. Cornerplot showing the posterior distributions for all the free parameters in the equilibrium chemistry retrieval. The inset shows the best fit 4 node Bézier spline P – T profile, with the $\pm 1\sigma$ bounds obtained from the posteriors, with the $\tau=2/3$ pressure levels for each wavelength overplotted in grey.

retrieval are shown in Figure D1, and the best fit values for each parameter and their $\pm 1\sigma$ uncertainties are shown in Table D1.

APPENDIX E: K_p - V_{sys} CONFIDENCE INTERVAL MAPS FOR INDIVIDUAL SPECIES

We follow the same steps as Smith et al. (2024) to assess the contribution from individual chemical species to the cross-correlation

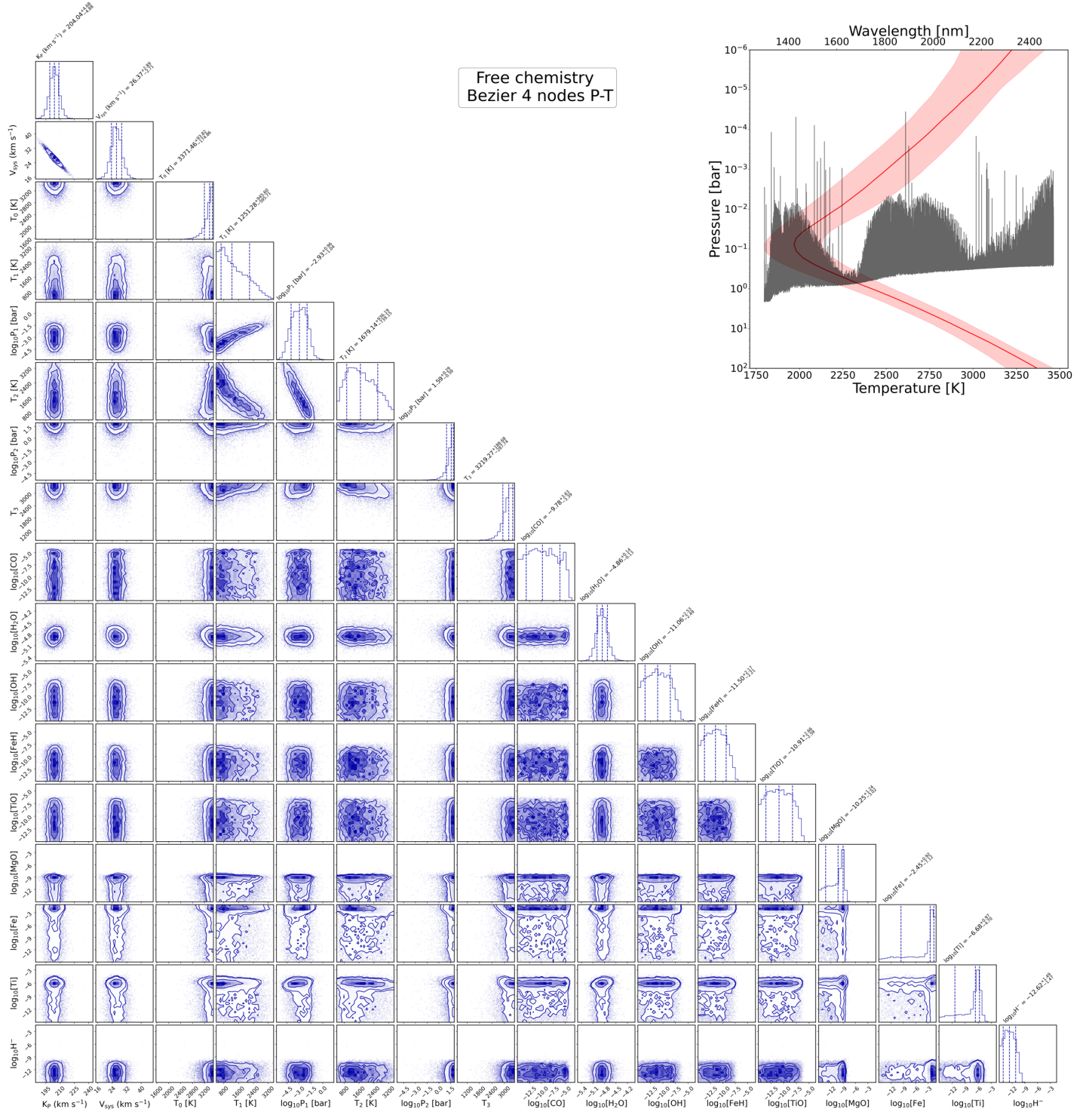


Figure A2. Same as Figure A1 but for the free chemistry retrieval.

signal by producing the $K_p - V_{\text{sys}}$ maps for each of them. In brief, we first compute a $K_p - V_{\text{sys}}$ log-likelihood map corresponding to the best fit model with the abundances of all the species set to their best fit values. Next, for a given species, we compute a model where the abundance of that species is set to a very small value (\log_{10} VMR = -30), and compute the $K_p - V_{\text{sys}}$ CCF map corresponding to this model. The log-likelihood map representing the contribution from

that species by itself is then computed as the difference between the all species log-likelihood map and the log-likelihood map with that species removed. The log-likelihood confidence intervals for each species in the equilibrium chemistry retrieval are shown in Figure E1. As expected, we find that the detected cross-correlation signal for the best fit retrieved model is primarily driven by H_2O , and none of the other species show any strong contributions by themselves

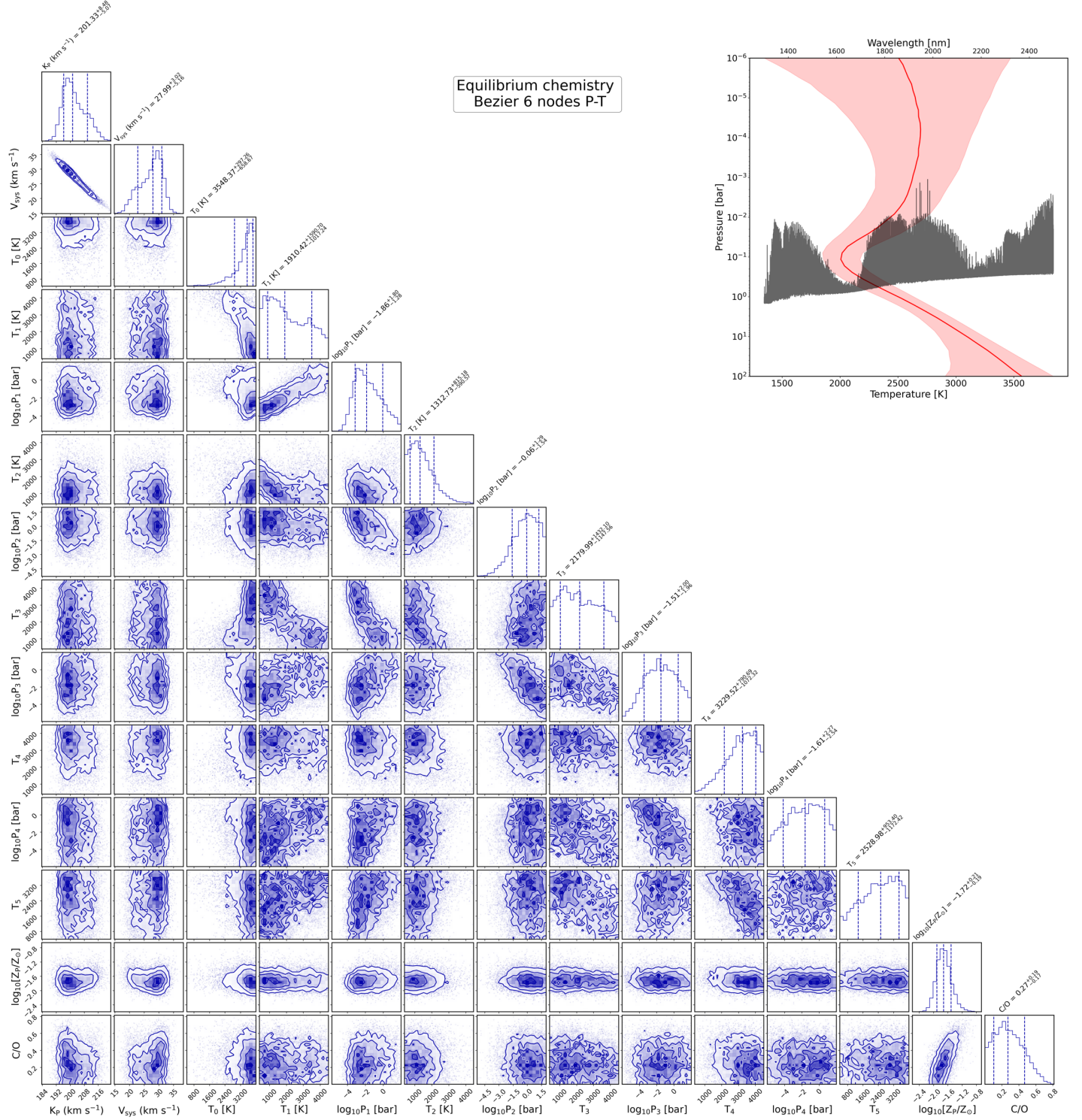


Figure B1. Same as Figure A1, but when using a 6 node Bézier spline P – T profile.

assuming there are no significant velocity shifts between different species.

This paper has been typeset from a \LaTeX file prepared by the author.

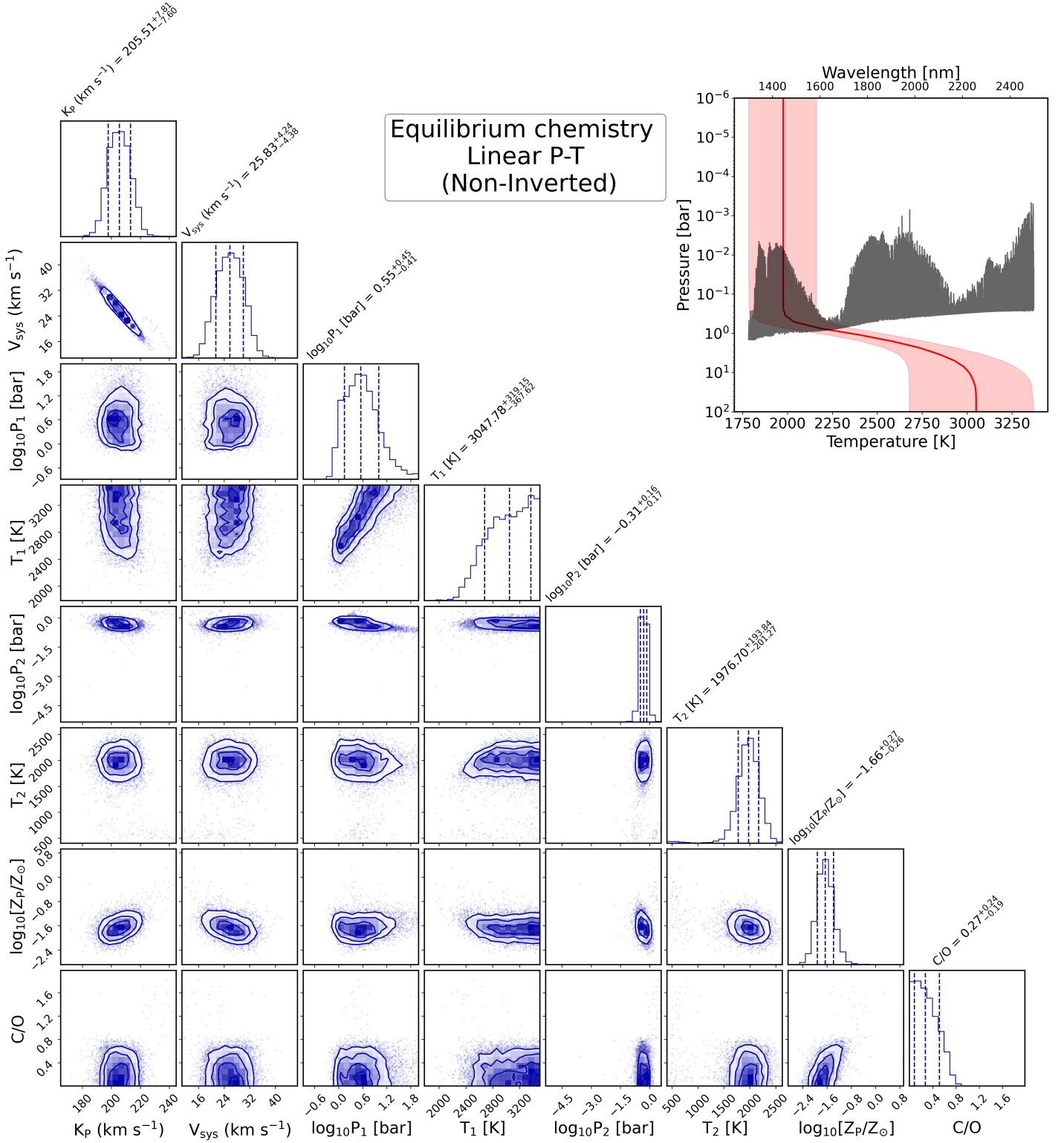


Figure B2. Same as Figure A1, but when using a linear P – T parametrization with no inversion.

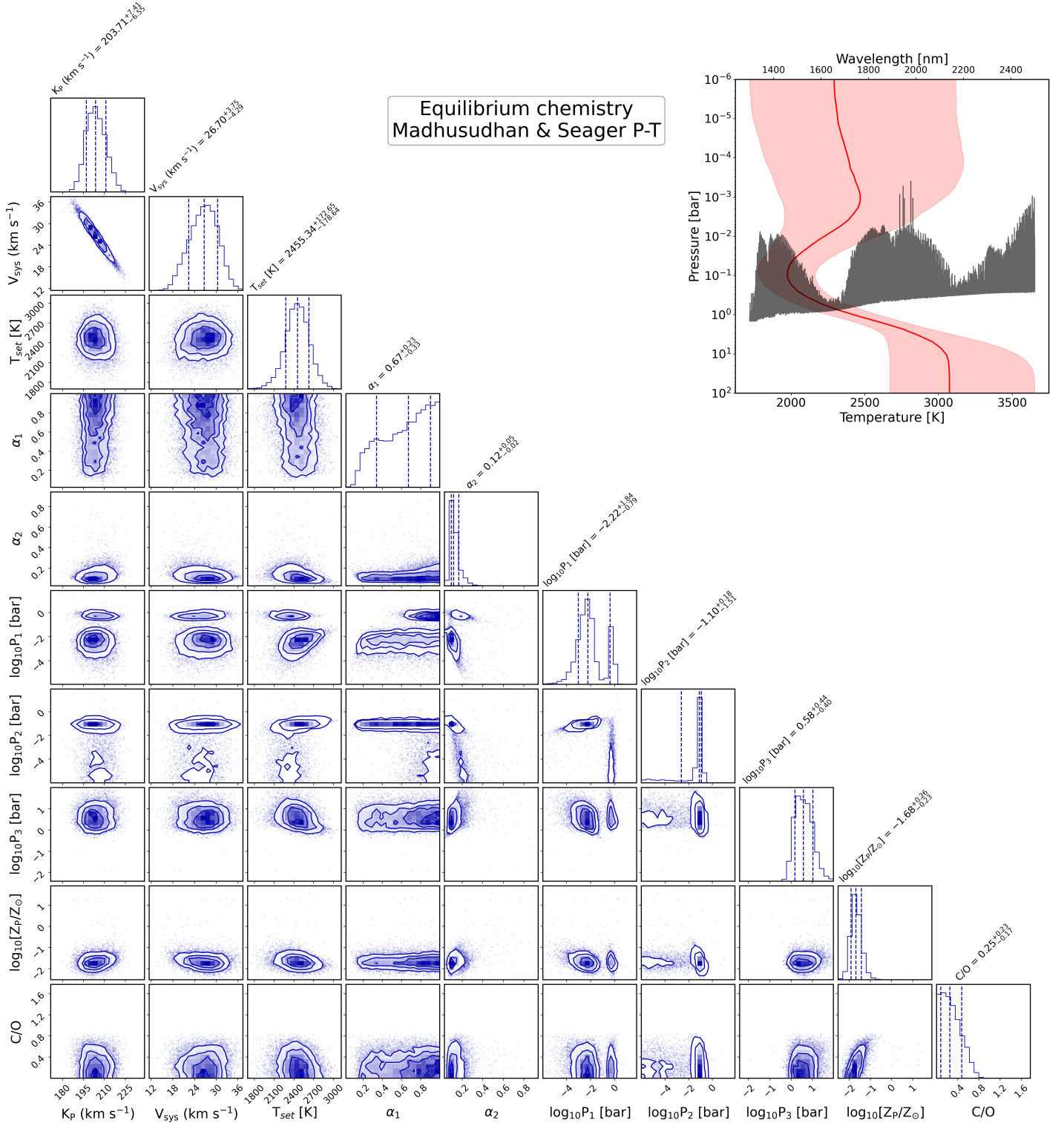


Figure B3. Same as Figure A1, but when using the [Madhusudhan & Seager \(2009\)](#) parametrization for the P – T profile.

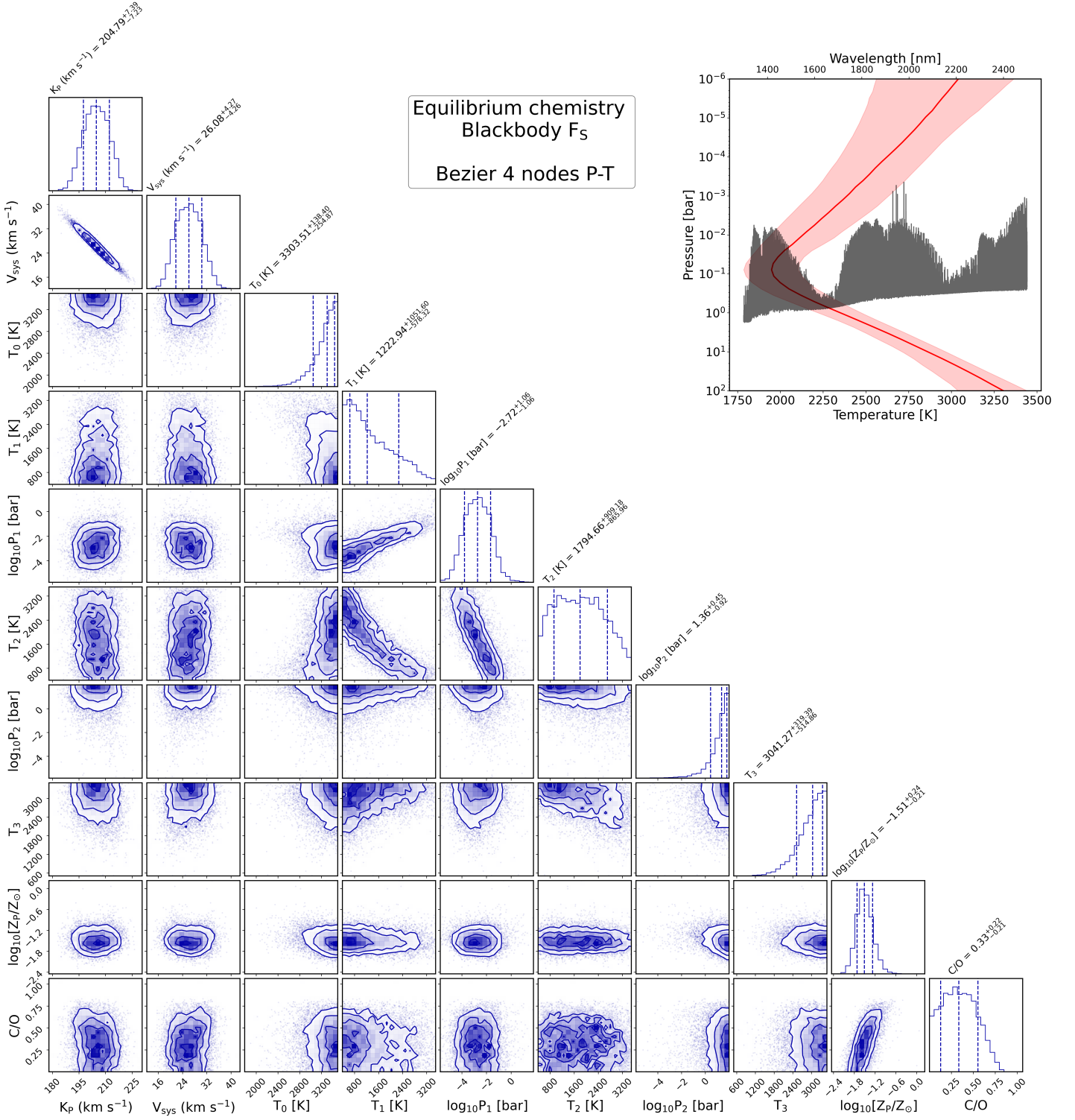


Figure C1. Same as Figure A1, but when using Blackbody corresponding to the T_{eff} of the host star instead of PHOENIX model for F_S when computing F_P/F_S .

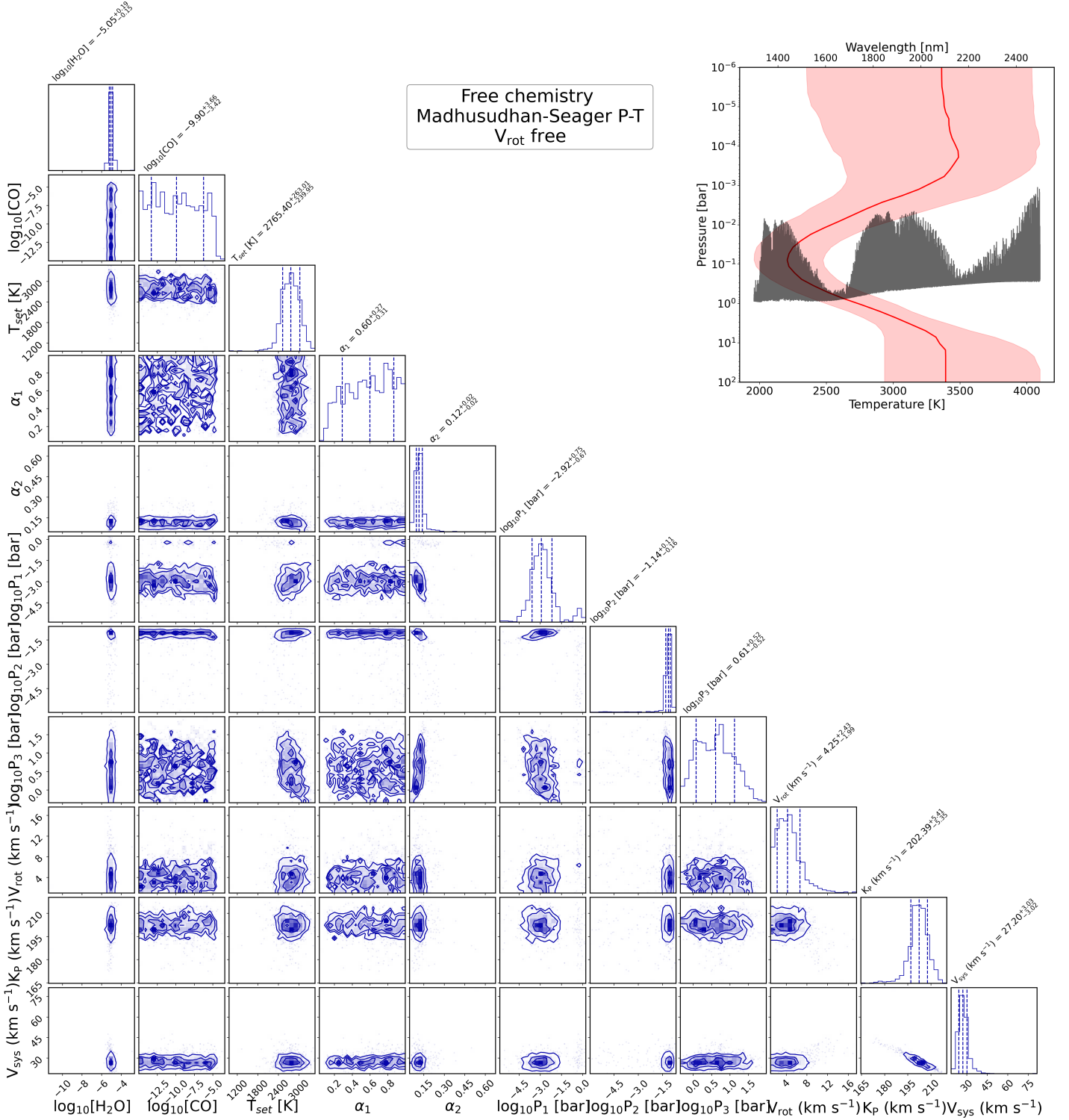


Figure D1. Same as Figure B3, but assuming free chemistry and also fitting for the planetary rotational velocity ($v_{\text{rot}} = v_p \sin i$).

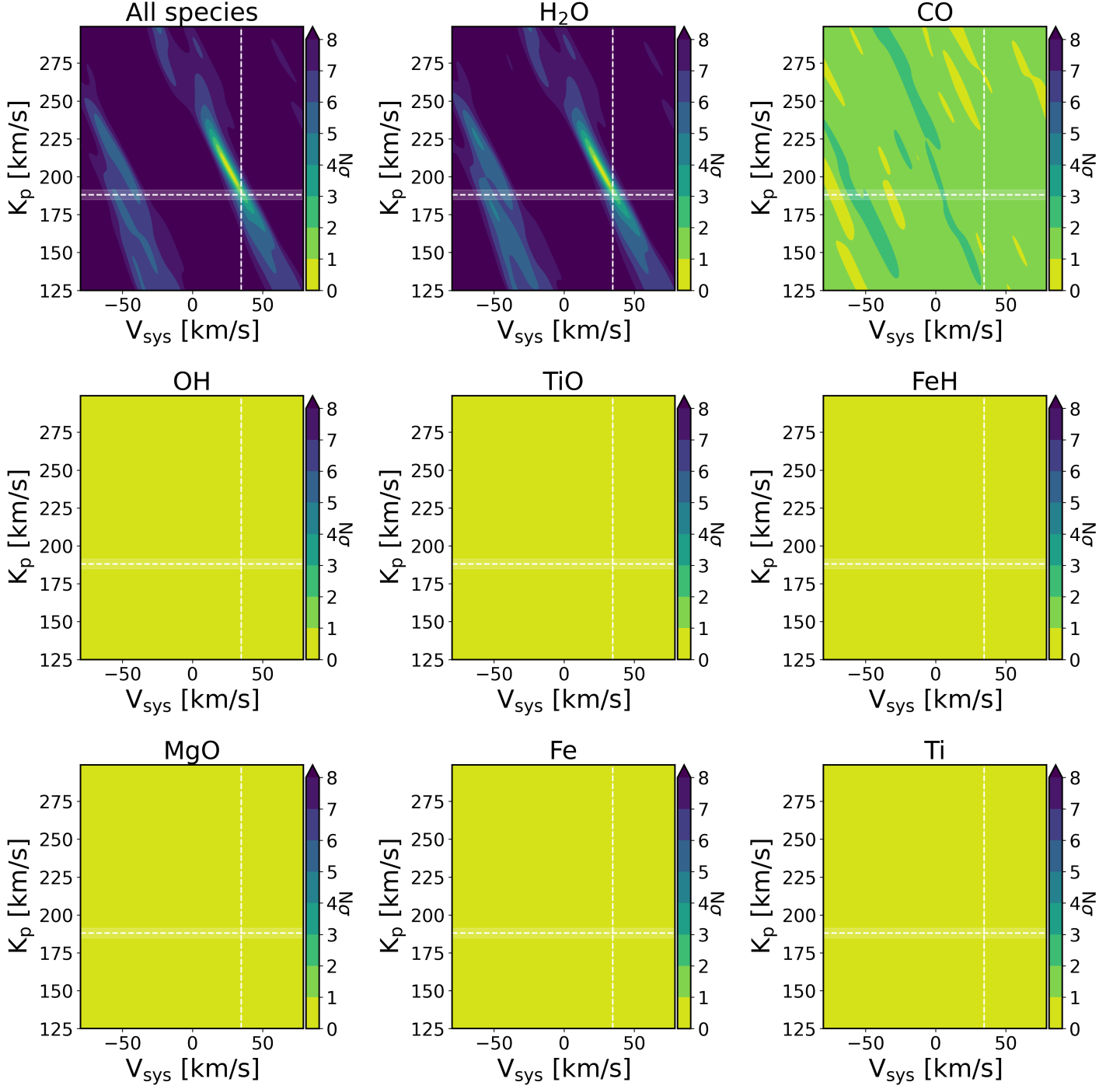


Figure E1. Log-likelihood derived confidence interval maps for individual species corresponding to their best fit abundances from the equilibrium chemistry retrieval described in Section 4. We find that except H₂O, none of the other species have any significant contribution to planetary signal detected via cross-correlation.

Table C1. Best fit and 1σ values for the parameters from equilibrium chemistry retrieval assuming F_S to be a blackbody spectrum corresponding to the T_{eff} of the star.

Parameter	Prior Bounds	Best-fit $\pm 1\sigma$
K_P (km s $^{-1}$)	[160.00, 250.00]	204.77 $^{+7.45}_{-7.27}$
V_{sys} (km s $^{-1}$)	[5.00, 50.00]	26.08 $^{+4.30}_{-4.28}$
T_0 [K]	[400.00, 3500.00]	3303.77 $^{+138.91}_{-255.54}$
T_1 [K]	[400.00, 3500.00]	1215.79 $^{+1062.63}_{-571.63}$
$\log_{10}P_1$ [bar]	[-6.00, 2.00]	-2.72 $^{+1.07}_{-1.07}$
T_2 [K]	[400.00, 3500.00]	1791.86 $^{+926.09}_{-870.88}$
$\log_{10}P_2$ [bar]	[-6.00, 2.00]	1.37 $^{+0.45}_{-0.94}$
T_3 [K]	[400.00, 3500.00]	3042.74 $^{+320.04}_{-523.37}$
$\log_{10}[Z_P/Z_\odot]$	[-6.00, 2.00]	-1.51 $^{+0.24}_{-0.21}$
C/O	[0.00, 2.00]	0.34 $^{+0.22}_{-0.21}$

Table D1. Best fit and 1σ values for the parameters from free chemistry retrieval with the [Madhusudhan & Seager \(2009\)](#) P – T profile, and also fitting for planetary rotational velocity ($v_{rot} = v_P \sin i$.)

Parameter	Prior Bounds	Best-fit $\pm 1\sigma$
K_P (km s $^{-1}$)	[160.00, 250.00]	202.39 $^{+5.41}_{-5.35}$
V_{sys} (km s $^{-1}$)	[10.00, 50.00]	27.20 $^{+3.03}_{-3.02}$
T_{set} [K]	[1000.00, 3500.00]	2765.40 $^{+263.01}_{-239.95}$
α_1	[0.02, 1.00]	0.60 $^{+0.27}_{-0.31}$
α_2	[0.02, 1.00]	0.12 $^{+0.02}_{-0.02}$
$\log_{10}P_1$ [bar]	[-6.00, 2.00]	-2.92 $^{+0.75}_{-0.67}$
$\log_{10}P_2$ [bar]	[-6.00, 2.00]	-1.14 $^{+0.11}_{-0.16}$
$\log_{10}P_3$ [bar]	[-6.00, 2.00]	0.61 $^{+0.52}_{-0.52}$
$\log_{10}[CO]$	[-15.00, -1.00]	-9.90 $^{+3.66}_{-3.42}$
$\log_{10}[H_2O]$	[-15.00, -1.00]	-5.05 $^{+0.19}_{-0.15}$
v_{rot} (km s $^{-1}$)	[1.00, 50.00]	4.25 $^{+2.43}_{-1.99}$